Version of Record: https://www.sciencedirect.com/science/article/pii/S0927025620306273
Manuscript_f8b5ec9b80345126e5ff9f7108a49c4d

Hydrogen solubility and diffusivity near surface of nickel single crystals: some implications of elastic energy

C. Traisnel*, A. Metsue, A. Oudriss, J. Bouhattate, X. Feaugas

La Rochelle Université, Laboratoire des Sciences de l'Ingénieur pour l'Environnement, UMR CNRS 7356, Avenue Michel Crépeau, 17000 La Rochelle, France.
**corresponding author: caroline.traisnel1@univ-lr.fr*

Abstract :

The three low index surfaces of nickel, {100}, {110} and {111}, have been investigated to question the crystallographic orientation impact on hydrogen diffusivity and solubility near the surface. Diffusion profiles from Top adsorption sites underlined that subsurface migration barriers were different from the bulk and vary depending on the crystallographic orientation, revealing a local anisotropic diffusive behavior. The local geometry change of the successive occupied octahedral sites due to surface relaxation and H incorporation have also been investigated using nickel atoms positions of relaxed structures. The surface contraction effect on local octahedral sites appeared to be comparable to a vacancy effect on its nearest neighboring sites, both in terms of spatial extend and contraction magnitude. The hydrostatic contribution to H incorporation seemed to dominate the associate internal elastic energy, leading to a good description of local H solubility with the available volume. Local anisotropy at the surface proximity in terms of diffusivity and solubility were contained within the first atomic layers.

Graphical Abstract :

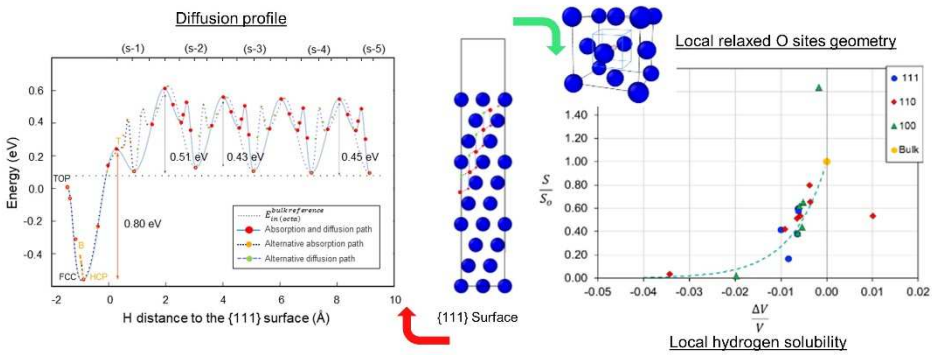

Key words: nickel; low index surfaces; hydrogen solubility and diffusion; displacement field; local elastic energy

1. Introduction

Hydrogen embrittlement (HE) impacts a very wide number of industrial fields. Indeed, from the aeronautical sector to the energetic one, by leading to premature failures, HE represents a challenging issue to the industry given its implications for metallic structures durability [1–5]. Yet, in corrosion, electrochemical treatments or ambient air processes, hydrogen omnipresence leads inevitably to its entrance in metals. Thus, as explained Kirchheim [6], two key properties must be mastered to avoid HE in an engineer point of view, that are H-solubility and H-diffusivity in the material. However, these properties are highly impacted by interactions with lattice defects [6,7]. Thus, to prevent HE phenomena, a good understanding of the synergy between the solute and the host matrix metallurgical state is fundamental. Moreover, the surface being the entrance to the material, such first order interactions are decisive regarding metallic structures lifespan in large number of environmental conditions and engineering applications.

A large number of experimental and numerical researches have already explored early H-surface interactions on metals [6,8–13], from adsorption step to absorption, and especially on nickel low Miller index surfaces [14–18]. These ones are targeted in this article since it is well established that a common surface corresponds to the combination of three compacts surfaces {100}, {110} and {111} with a specific number of defects, like kinks, edges or vacancies [19]. The high reactivity of hydrogen located at the surface, and above all in subsurface sites, has also been enhanced in the hydrogenation and hydrogenolysis research field, especially on Ni{111} orientation due its high catalysis properties [20]. This point has been reported, among others, by Greeley *et al.* offering in their paper [16] a global overview of both experimental and theoretical studies previously undertaken in order to understand the specificity of Ni surface and subsurface sites. H-surface interactions are then not only the matter of HE, which expands all the more the scope of such studies, while many points remain unexplored.

To some extent, a perfect surface can already be considered as a defect due to the symmetry break and the surface atoms relaxation implied. Generating an elastic distortion of interstitial sites, H-solubility and diffusivity must evolve depending on the distance to the surface. In this paper will be identified the crystallographic orientation impact on the subsurface extent and the associated consequences on H local solubility. The subsurface being defined here as the transition zone between the surface and the bulk. This theoretical study will further be used as a comparison reference in a following paper dealing with electrochemically H-charged nickel {100}, {110} and {111} un-deformed samples at ambient temperature, where eletroadsorbed H corresponds to the Over Potential Deposited Hydrogen (OPD-H) highlighted by Conway *et al.* [21]. The upcoming comparison of subsurfaces depth obtained by both approaches, thanks to the expanse of the local H diffusion coefficient evolution, will enable us in the future to complete our theoretical model with punctual defects.

To do so, we need to obtain numerically the H diffusion path involved during cathodic electrochemical charging tests (OPD-H), thus from unstable Top adsorption sites (as demonstrated [22,23]). However, if numerical absorption paths have long been identified from gaseous H_2 dissociative adsorption and absorption from Hollow stable sites, the corresponding path OPD-H from aqueous phase, even if similar, remained only suggested. Then we first aimed at completing the literature on surface migration energies from all possible adsorption site for perfect Ni {100}, Ni {110} and Ni {111} surfaces. We could therefore confirm the most probable path for electroadsorbed H from a Top site for each crystallographic orientation. These paths have been determined for low H coverage rates (1/4) for two reasons. First, to avoid H-interactions that affect the migration energies values [15,16]. Second, Bokris *et al.* established relations between H_2 fugacity and experimental surface conditions (overpotential, coverage) [24]. And, as reported in a previous study, DFT calculations present solubility results in good agreement with electrochemical experiments for a fugacity under 400 atm [25], which corresponds to low H coverages. Eventually the impact of elastic displacement fields associated with the surface elastic relaxation has been questioned depending on the orientation. Consequently the interstitial octahedral sites changes of geometry have been correlated to the hydrogen apparent solubility in these sites and discussed in terms of elastic energy [26]. To this end, we went back to the definition of an octahedral site, using nickel atoms exact positions after relaxation calculations. Atomic scale calculations ensure here a significant complement to experiments enabling to elucidate some mechanistic details that would be nearly impossible to identify only through experimental processes.

This paper is organized as follows. In Section 2 the computational details are given as well as methods to identify the minimum energy path and to calculate local elastic energy in octahedral sites. In Section 3, the hydrogen diffusion profile from oriented surfaces and the consequent local diffusion coefficients are discussed. Then, an analysis between the orientation impact on local hydrogen solubility is provided in Section 4. This section will first uncouple surface induced and hydrogen induced displacement fields on local elastic energy, to finally bind the local octahedral site geometry with global incorporation energy. Conclusions are drawn in Section 5.

2. Method

2.1. Computational details

The calculations involved this study were atomic-scale based and used the density functional theory (DFT) framework limited at T=0K [27,28] with the spin-polarized implementation of the Quantum ESPRESSO package PWSCF code [29]. To describe the nickel and hydrogen ion-electrons interactions, pseudopotentials built with the projector augmented wave method (PAW) were handled [30]. The plane wave cut off was set to 816 eV with a 0.027 eV Fermi-Dirac smearing to broaden the electronic density of states, as adopted in previous studies [31,32]. In our calculations the exchange-correlation effect was

approximated by the generalized gradient corrections (GGA) in the formulation of Perdew, Burke and Ernzerhof (PBE functional) since it presents closer results to experiments regarding nickel primitive cell volume and cohesion energy than LDA functional [31]. The irreducible Brillouin Zone sampling for each surface was based on the Monkhorst-Pack technique [33], with a k-mesh density equivalent to 14×14×14 for the Ni bulk conventional cell. This density also corresponds to the sampling (50/x) × (50/y) × (50/z) suggested by Tran *et al*. [34] in their surface energy calculations.

2.2. Simulation cells setup

The approach involved to represent systems with broken symmetry like surfaces is the slab model [34,35], wherein a nickel supercell oriented is generated and presents the surface of interest. Starting from the nickel conventional unit cell, lattice vector transformations were realized to find for a given surface its oriented unit cell (OUC) as explained by Tran *et al.* [34]. The ***x*** and ***y*** lattice vectors obtained for each OUC were parallel to the corresponding low Miller index plane {hkl} ({100}, {110} and {111} in this study), held by z. After that, the unit cell were repeated along ***x, y,*** z axis and vacuum was finally added along z. For each of the three surfaces, the OUC repetition size and the vacuum height necessary were determined by the convergence of two energies:

- the surface energy γ^{hkl},
- the H incorporation energy E_{in} in an octahedral site positioned the middle of the Ni stacking along z (in other words, for H position along z equal to $z_{Ni}/2$, z_{Ni} being the height of the slab without vacuum). This energy needs to reach the bulk H solution energy so that the middle of Ni stacking could be reasonably assimilated to the bulk material.

These energies were calculated respectively using the following equations :

$$\gamma^{\mathrm{hkl}} = \frac{(E_{slab}^{hkl} - E_{bulk}^{hkl}\, n_{slab})}{(2S_{slab})} \tag{1}$$

$$E_{in} = E_{slab+H}^{hkl} - E_{slab}^{hkl} - \frac{1}{2}E_{H_2} \tag{2}$$

Where E_{slab}^{hkl} the slab total energy representing the {hkl} surface, E_{bulk}^{hkl} the energy per atom of the corresponding oriented bulk (same slab without vacuum), and n_{slab} is the number of atoms in the slab. E_{in} is the H solution energy in a given interstitial (or adsorption) site, E_{slab+H}^{hkl} is the energy of the {hkl} slab with an hydrogen atom incorporated at that position, and E_{H_2} the dihydrogen molecule energy obtained by Joannopoulos *et al*.'s method [35]. Once the {100}, {110} and {111} supercells created, H adsorption energy computations on each surface adsorption site were first held using equation (2), by structure relaxation calculations at constant pressure fixed at 0 GPa. Then, hydrogen incorporation energy was determined the same way for each octahedral (O) and tetrahedral (T) interstitial site from the first subsurface site (s-1) towards the center (=bulk). The convergence was achieved when total forces acting on the atoms were less than 2.6×10^{-4} eV/Å and energy differences on electronic charge density less than 1.4×10^{-8} eV.

2.3. Minimum energy path identification

Next, we desired to identify the hydrogen Minimum Energy Path (MEP) from a Top adsorption site to the subsurface and then towards the bulk (*i.e.* supercells center), to obtain the most probable absorption and diffusion paths. In this regard, nudged elastic band calculations (NEB) based on transition state theory were performed [36] with the climbing image method [37], using for each section at least 5 images. Our convergence criteria was a force error inferior to 0.07 eV/Å on each image. Starting from the Top adsorption site, to get the most likely absorption path for the three {100} {110} {111} orientations, all the possible paths to reach the first subsurface site (s-1) were investigated to find those with the less energetic migration energies. Wimmer *et al*. evidenced that H diffuses from an octahedral site to another through a tetrahedral intermediate site in fcc materials [38]. Our climbing image NEB calculations were thus led to find the H transition states between each O-T diffusion sections and the corresponding migration energy (E_{mig}) [38] from the subsurface towards the bulk. We could then draw the H diffusion profile from each surface Top site to the bulk, showing the H migration energy evolution and, by extension, the diffusion coefficient evolution depending on H distance to the surface, and depending the surface crystallographic orientation. Tunneling, whose effect can be sizeable at very low temperatures [39–42], was not taken into account in this work because we aim at comparing later our results to electrochemical experiments at ambient temperature.

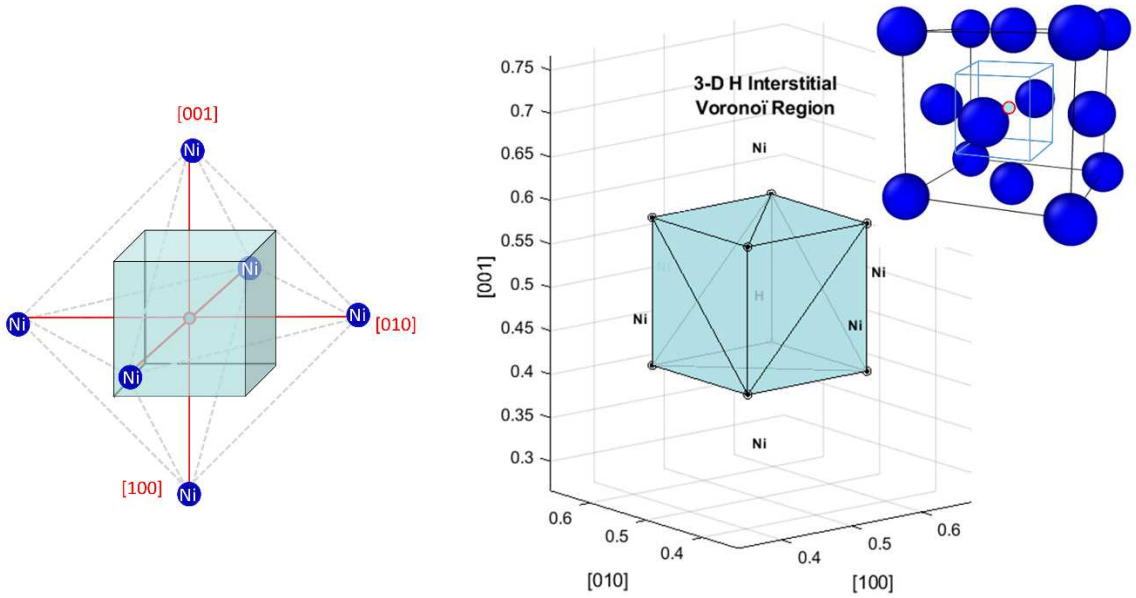

Figure 1 : Schematic representations of an octahedral site in unstressed nickel conventional lattice using Delaunay triangulation (grey dotted lines), with the associated Voronoï volume (blue cubic shape) and the crystallographic axes.

2.4. Octahedral sites geometry and internal elastic energy

In this last part we assessed the effects of {100}, {110} and {111} oriented surfaces on H solubility in octahedral sites. As H-local solubility is generally appropriately related to an internal hydrostatic stress

[43–48], we had to characterize each site's geometry accurately, starting with their volume. To do so, for each supercell we had to change of base to express relaxed nickel atoms positions in a common basis of orthonormal axes ($\boldsymbol{e_1}$,$\boldsymbol{e_2}$,$\boldsymbol{e_3}$) respectively oriented in [100], [010] and [001] directions. As schematized in Figure 1, each octahedral site is located in between 6 Ni neighbors atoms that are conventionally positioned on these axes. By using the Voronoï method, the available volume of each site can be easily evaluated. As a reference, for unstressed Ni structures, these sites present a cubic shape and a volume of 5.46Å^3 when vacant and 5.81Å^3 otherwise. A volume change would mean an internal hydrostatic strain, while a deviation to this cubic geometry (if axes no longer match [100], [010] and [001] directions) would represent a distortional contribution. This last contribution might be unneglectable, above all close to the surface, as it has already been proved near grain boundaries [43] or near dislocation cores [49]. Two separated steps were necessary to decouple the surface induced strain and then hydrogen induced strain within each site depending on their distance to the surface. We assumed that the strain was the same for all sites at a same z-distance to the surface, so that we assessed it for only one site at a given z position. Then, the first step was to evaluate the local deformation of octahedral sites without hydrogen depending on their proximity to the {hkl} surface (step 1 presented in Figure 2a). Here we took as a reference the octahedral site of the unstressed nickel conventional cell. We determined the local displacement field $\vec{u}$ generated by each surface orientation with the relaxed Ni positions obtained after structure optimization calculations. This led to the associated deformation matrix $\bar{\bar{\epsilon}}$ since for infinitesimal deformations the tensor can be expressed as follows:

$$\bar{\bar{\epsilon}} = \frac{1}{2}\left(\nabla\vec{u} + \nabla\vec{u}^{T}\right) = \begin{pmatrix} \epsilon_{11} & \epsilon_{12} & \epsilon_{13} \\ \epsilon_{12} & \epsilon_{22} & \epsilon_{23} \\ \epsilon_{13} & \epsilon_{23} & \epsilon_{33} \end{pmatrix}_{(\vec{e_1},\vec{e_2},\vec{e_3})} \tag{3}$$

The hydrostatic and distortional contributions to internal elastic energy E_{el} within these sites were estimated due to their shape and volume change making the approximation of isotropic elasticity. The volume elastic energy is given by the following relation:

$$E_{el} = \oint \sigma_{ij} d\epsilon_{ij} = \frac{1}{2}\sigma_{ij}\epsilon_{ij} \tag{4}$$

This energy can be decomposed in hydrostatic E_{el}^{m} and distortional E_{el}^{d} parts as follows

$$E_{el} = E_{el}^{m} + E_{el}^{d} \tag{5}$$

Where each of these terms can be expressed:

$$E_{el}^{m} = \frac{3}{2}\sigma_m\epsilon_m = \frac{9B}{2}[\epsilon_m]^2, \qquad with\ \epsilon_m = \frac{1}{3}Tr(\bar{\epsilon}) = \frac{\sigma_m}{3B} \tag{6}$$

$$E_{el}^{d} = \frac{1}{2}\sigma_{ij}^{d}\,\varepsilon_{ij}^{d} = G\epsilon_{ij}^{d}\epsilon_{ij}^{d} = \frac{3}{2}G\left[\epsilon_{eq}^{d}\right]^2, \qquad with\ \sigma_{ij}^{d} = 2G\epsilon_{ij}^{d} \tag{7}$$

These volume energies where eventually multiplied by the reference nickel octahedral volume. *B* and *G* are respectively the nickel bulk and shear moduli. Their values were determined thanks to previous DFT calculations of bulk nickel elastic constants [50] and reduced to the scope of isotropic elasticity. Hence, $B = (C_{11}+2C_{12})/3$ and $G=C_{44}$. The ϵ_m term expresses the change of volume in comparison with the reference site, and ϵ_{eq} the generalized Von Mises equivalent strain:

$$\epsilon_{eq}^{d} = \sqrt{\frac{2}{3}\varepsilon_{ij}^{d}\varepsilon_{ij}^{d}} = \frac{2}{3} \times \frac{\sqrt{(\epsilon_{11}-\epsilon_{22})^2 + (\epsilon_{22}-\epsilon_{33})^2 + (\epsilon_{11}-\epsilon_{33})^2 + 6(\epsilon_{12}^2 + \epsilon_{23}^2 + \epsilon_{13}^2)}}{\sqrt{2}} \quad (8)$$

Second, the same procedure was followed with the inclusion of a hydrogen atom in these sites to assess their accommodation to H introduction (step 2 presented in Figure 2b). In other words, the sites analyzed during step 1 became the new reference for themselves with one hydrogen atom inside. Using the displacement field identified after structure relaxation calculations, we got the corresponding $\bar{\bar{\epsilon}}$ matrix, giving us by extension the local excess of elastic energy due to H insertion. The volume used here for energy calculations was the reference one for each site (*i.e.* equivalent site without H).

Note that for this second step our strain matrix has systematically been corrected by subtracting the difference between the stain matrix obtained for the corresponding oriented bulk due to H insertion and the conventional cell supercell (3×3×3) one to H insertion. Indeed, some discrepancies were observed meanwhile the same strain matrix was expected for bulk supercells. Those were mainly due to the k-mesh taken as far as possible with the same density for each orientation. Yet, it appeared that a finer one might be required for orientations different from the conventional {100} one to consider displacement fields even more precisely. In addition, the H concentration was different for each supercell, and with a density much higher in $\boldsymbol{x}$ and $\boldsymbol{y}$ directions than in the $\boldsymbol{z}$ one. Instead, for the (3×3×3) conventional supercell the H density was the exact same in the three directions. This correction enabled us to compare the strain matrices of each orientation with the same bulk reference.

a)

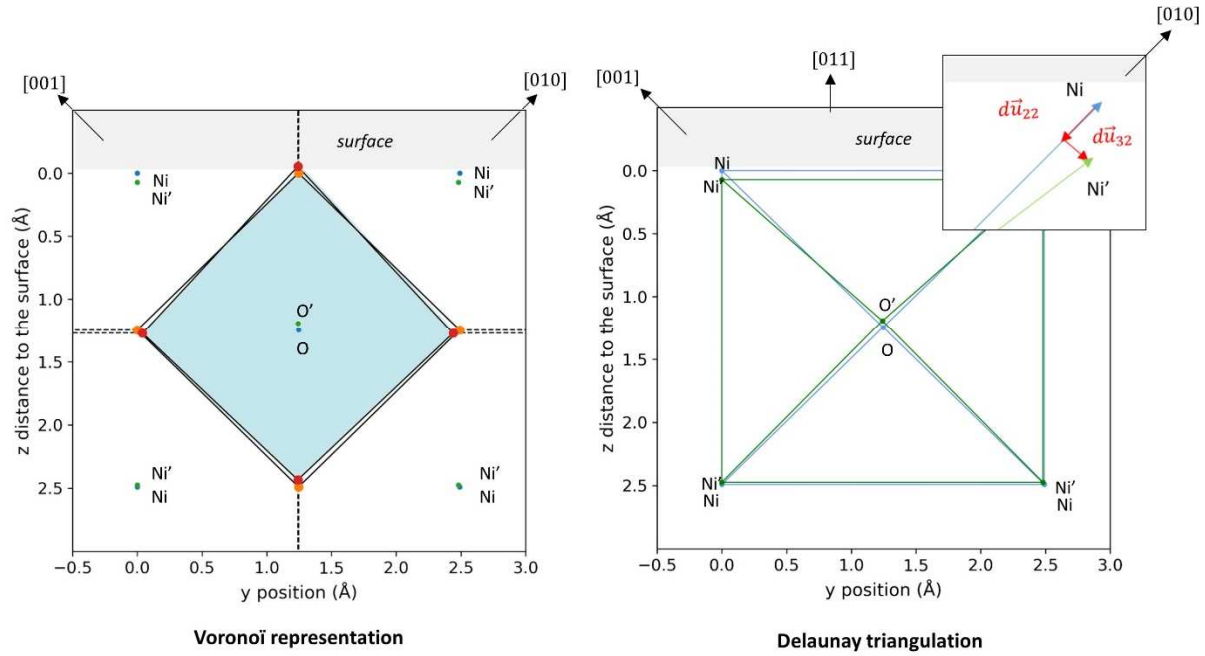

b)

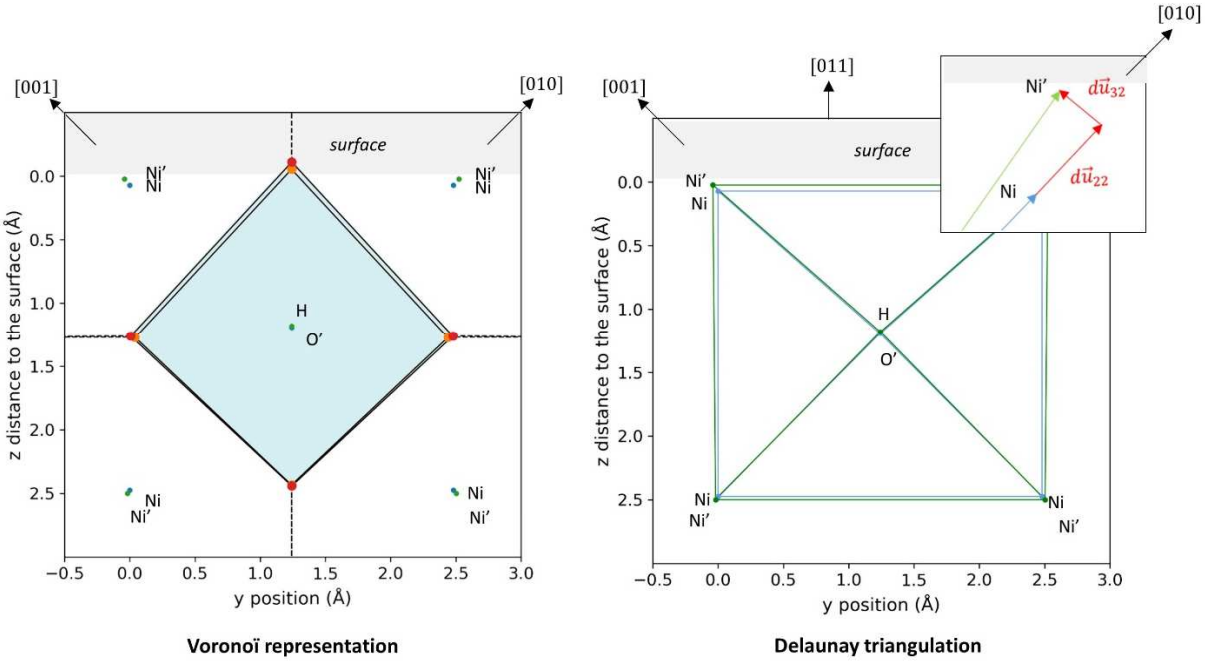

Figure 2 : a) 2D-scheme of an (s-1) vacant site in case of {110} surface representing step 1: assessing the volume and the shape change of the octahedron due to the surface, without hydrogen. Voronoï representation enables to see the available volume, while Delaunay triangulation permits to visualize the displacement field components in ($\boldsymbol{e}_1$,$\boldsymbol{e}_2$,$\boldsymbol{e}_3$) base. Ni represent the atoms positions of the reference (blue) [= site in unstressed nickel conventional cell] and Ni' (green) represent the atoms of the investigated z-site, with the respective centers O and O'. b) Step 2 : assessing the volume and the shape change of the octahedron due to hydrogen insertion. Ni now represent the atoms positions of the reference (blue) [= equivalent z-site without H] and Ni' (green) represent the same atoms displaced by H.

3. Hydrogen evolution from the surface to the bulk

3.1. Oriented surfaces and hydrogen adsorption

Table 1 : Surface energies results compared to previous computed values from literature

	{100} surface	{110} surface	{111} surface
γ^{hkl} *present work (eV /Å²)*	0.142	0.145	0.122
γ^{hkl} *previous DFT studies (eV /Å²)*	0.138 [a] , 0.151 [b] 0.140 [c], 0.137 [d] , 0.139[e]	0.143 [a] , 0.148 [b] 0.144 [c] , 0.140 [d]	0.120 [a] , 0.126 [b] 0.121[c] , 0.120 [d], 0.120[e]

[a] *[34]* [b] *[51]* [c] *[52]* [d] *[53]* [e] *[54]*

For the three slabs, the vacuum height was fixed at 6 Å and Ni atoms stacking of at least 5 Å along the normal to the surface was sufficient to ensure a surface energy convergence within less than 1 meV/ Å². The corresponding results presented in Table 1 are in good agreement with values obtained in previous DFT studies [34,51–54]. Correcting these surface energies with Zero Point Energy (ZPE) effects brought a change of less than 1 meV on our values. However, when hydrogen is inserted, the slabs need to be enlarged in the three directions by multiplying the corresponding OUC. This ensures interactions between adjacent hydrogens are negligible, as surface effects when hydrogen is in the middle of the Ni stacking along z. For the {100} surface, the repetition $2 \times 2 \times 6$ of the {100} OUC was selected. For the {110} surface, $2 \times 2 \times 7$ repetition of the {110} was used. Eventually, for the {111} surface, a $2 \times 1 \times 3$ repetition of the pattern was enough. For each of these supercells, the E_{in} value for hydrogen inserted in the middle of Ni stacking along z (bulk position in Figure 3) converged within 0.01 eV in comparison to the reference bulk value of 0.11 eV [32]. This precision being better than one can obtain experimentally, it is reasonable to consider that the middle of these supercells at 0K behaved similarly to Ni bulk with hydrogen. The resulting supercells after both surface and H incorporation energies convergence are represented in Figure 3 and were used for all the results presented in this study.

As already reported in several studies, numerical and experimental [15,53–58], due to the symmetry break imposed by the vacuum, both a contraction and a dilatation of the first Ni layers along z were observed for the three orientations due to the symmetry break. This resulted in lattice spacing changes as summarized in Table 2. The global behavior was the same for each orientation, that is to say, a relative lattice spacing reduction between the two first layers ($\Delta d_{12}<0$) and an increase for with the following layer ($\Delta d_{23}>0$). Our results fit within the numerical accuracy to those obtained in previous DFT studies mentioned above, both in terms of values as well as the orientations ranking. They also fit closely to values obtained by Low Energy Electron Diffraction (LEED) technique or Medium Energy Ion Scattering (MEIS) [56–58]. The Ni {110}-oriented surface is much more impacted due to the highest number of metallic Ni broken bounds (5) in comparison to the other orientations (4 for Ni {100} and

only 3 for Ni {111}). It is by extension also the most reactive orientation and thus presents the highest surface energy (Table 1). On the contrary, Ni {111} is the most compact surface, so the less reactive and the least impacted by surface relaxation and lattice changes.

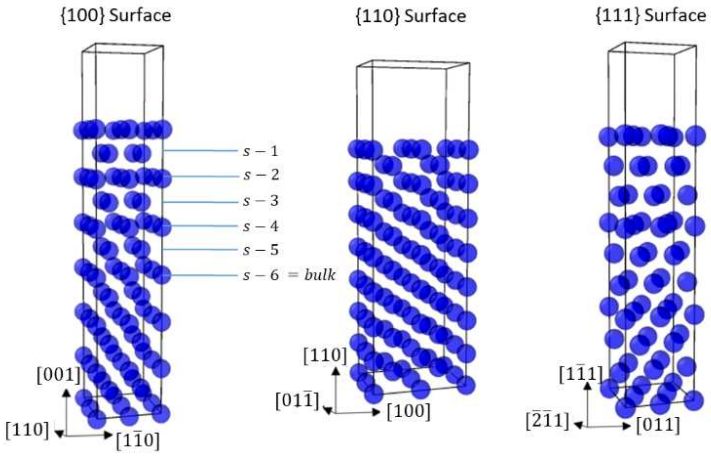

Figure 3 : Clean Ni {100}, {110} and {111} slabs, with on Ni {100} slab octahedral interstitial sites positions along *z* indicated

Table 2 : Lattice spacing changes between the two first Ni layers, and between the second and the third layers

	{100} surface		{110} surface		{111} surface	
	Δd_{12}	Δd_{23}	Δd_{12}	Δd_{23}	Δd_{12}	Δd_{23}
Present work	-2.8%	+1.5%	-9.9%	+2.9%	-1.0%	+0.2%
Previous DFT studies	-3.6% [a]	+1.0% [a]	-10.4% [a]	+1.8% [a]	-1.2% [a]	+0.1% [a]
	-3.6% [b]	+1.4% [b]	-10.3% [b]	+3.2% [b]	-0.9% [b]	+0.0 [b]
	-3.74% [d]	+0.55% [d]	-		-1.31% [d]	-0.09% [d]
	-2.7% [e]		-6.5% [e]		-1.5% [e]	
Experimental values	-3.2% [f]	-	-8.7% [c]	+3.0% [c]	0±1% [g]	-

[a] *[15]* [b] *[53]* [c] *[57]* [d] *[54]* [e] *[55]* [f] *[56]* [g] *[58]*

Nickel low Miller index surfaces present 3 types of high symmetry adsorption sites Top, Bridge (B) and Hollow (HL), all represented in Table 3. These are distinguished by their coordination number, respectively: 1, 2 and 3 (or 4). Ni {110} presents two kinds of Bridge sites : Long Bridge (LB) and Short Bridge (SB), as well as two Hollow sites : Pseudo Three-fold (PT) bounded to 3 Ni surface atoms, and Four-fold (4F) bounded to 4 Ni surface atoms. Ni {111} presents also two Hollow sites : HCP with a Ni atom of the layer just below the surface, and FCC whose first Ni below is from the second Ni layer under the surface.

Table 3 : Adsorption energies (eV) of atomic H on high-symmetry sites for a ¼ coverage (θ) with a schematic representation on each supercell's surface. The brighter are the Ni atoms, the deeper they are. Then the darkest belong to the surface

	{100} surface		{110} surface		{111} surface
Top	0.005		0.053		-0.033
	0.016 [a] , 0.06[b]		0.086 [a] , 0.11[b]		0.001 [a] , -0.13[b] , -0.01[c]
Hollow	-0.523	PT 4F	-0.438 -0.223	FCC HCP	-0.596 -0.586
	-0.567 [a] , -0.546[b]	PT 4F	-0.450 [a] , -0.37[b] -0.226 [a] , -0.24[b]	FCC HCP	-0.598 [a] , -0.486[b] , -0.61[c] -0.587 [a] , -0.486[b], -0.60[c]
Bridge	-0.431	LB SB	-0.381 -0.413		-0.454
	-0.457 [a] , -0.39[b]	LB SB	-0.409 [a] , -0.34[b] -0.391 [a] , -0.31[b]		-0.456 [a] , -0.37[b], -0.47[c]
Schematic view	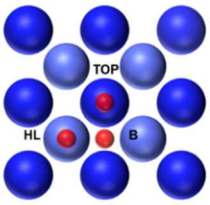		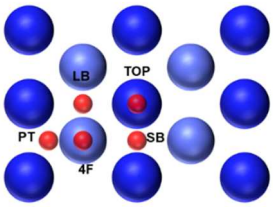		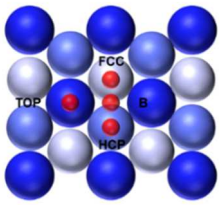

[a] *[15]* [b] *[17]* [c] *[16]*

For each of three supercells built, the surface was composed of 4 Ni atoms. Hydrogen adsorption energies were then calculated for a θ=¼ coverage and the corresponding results are summarized above, in Table 3. Top sites involved in electrochemical OPD-H reactions [22] present the lowest coordination and are logically the most energetic ones. Meanwhile Hollow sites, involved in UPD-H reactions, by offering the highest coordination to H, are the very stable, with adsorption energies close to chemisorption. For the three surfaces, adsorption energies were globally in quite good agreement with those reported earlier by Bhatia *et al.* [17] and Kresse *et al.* [15], or Greeley *et al.* for the {111} orientation [16]. Nevertheless, some discrepancies or difficulties must be reported about the Bridge sites. For Ni {110}, in previous studies LB were found more stable than SB [15,17], and the reverse was highlighted here (even if adsorption energies remained quite close). As the relaxation conditions were different, as well as the vacuum height, additional tests have been led using the same supercell as in Kresse *et al.*'s work [15] with 5 Ni layers and a 10Å vacuum. However, with this new supercell, SB remained more stable than LB, both by fully relaxing the system or allowing only the two first Ni layers to relax. The difference obtained between the two relaxing conditions was of 3 meV for LB and 1 meV for SB, which still does not explain our higher discrepancies. Yet, the fact ZPE corrections were not used for our calculations has been questioned since it can be unneglectable for light adsorbed species such as H. In the example of Bhatia *et al.*'s supercells, the impact of ZPE corrections could reach 0.12 to 0.19 eV for the most stables sites. In Greeley *et al.*'s study [16] ZPE effect reduced H adsorption energy on fcc to -0.56 eV instead of -0.61 eV, which revealed a better correlation to experimental data

of -0.49 eV and -0.50 eV respectively from references [59] and [14] for the lowest hydrogen coverage both obtained by temperature-programmed desorption (TDP). Nevertheless, we assume ZPE effects should not change the order between LB and SB H-adsorption energy. The differences might lie then in the convergence criteria or the computational details such as the k-mesh density or the functional to estimate the exchange-correlation energy. About H adsorption on a Ni {111} B site, forces acting on Ni atoms remained higher than 2.6×10^{-4} eV/Å, so that we took the energy with the lowest total force on all atoms ($5.2\ 10^{-3}\times$eV/Å). As reported before [16], this site is not a true local minimum. Rather unstable, it coincides with the transition state between FCC and HCP sites, as it will be seen in section 3.2.3. However, the accepted adsorption value was among the closest to cited references for this site.

3.2. Hydrogen diffusion paths

Once the supercells determined, we used NEB method to compute surface migration energies at 0K. Firstly, between each adsorption site to find the most probable surface diffusion path from Top sites. Secondly, all the possible absorption paths towards the first octahedral subsurface site (O (s-1)) or tetrahedral if closer to the surface ({100} and {111} supercells) were also investigated. Eventually, migration energies for each O-T sections towards the bulk were computed to obtain the whole diffusion path.

3.2.1.Ni {100}

For the {100} orientation, T sites are exactly positioned between two O sites along z. Since s-1, s-2, s-3, (etc.) notation considers only O sites, the T sites were positioned versus the surface with the following notation: s-0.5, s-1.5, etc. Given the reported results in Table 4, from a Top site atomic H can very easily fall into a nearby Hollow or Bridge site. However, the NEB calculations never managed to converge for a complete diffusion path directly from Top to O(s-1), which means (given the distance to browse) that hydrogen will necessarily pass through other sites before, meanwhile the calculation managed to converge for the T(s-0.5) above. But, since no energy is required to reach B and HL surface sites, atomic hydrogen will most probably rather fall first in one of these sites for a ¼ hydrogen surface coverage. As long as from a B site absorption energy is higher than from a HL one, then the absorption would rather happen from this last one, letting the B site behaving like a transition one as reported by [17]. In addition, from B or HL to O(s-1), the T site always seemed to be occupied in between, which explains (T) in Table 4. Globally, the migration energies obtained were slightly lower than in the mentioned previous studies [15,17] since we worked with larger supercells and fully relaxed systems [39]. The most important energy value difference highlighted being for absorption from HL to O(s-1) site is due to the fact H occupied a (T) site closer to the surface in between in our case.

Table 4 : {100} Surface migration energies and absorption energies (eV) of atomic H

From \ *To*	*Top*	*Hollow*	*Bridge*	*T (s-0.5)*	*O (s-1)*
Top	x	0.00	0.00	0.78	-
Hollow	0.53	x	0.09 *0.110* [a] *0.18* [b]	0.96 *1.13* [b]	(T) 1.16 *2.48* [b]
Bridge	0.44	0.00 *0.026* [b]	X	1.22	(T)
T (s-0.5)	0.38	0.04	0.38	x	0.10
O (s-1)	-	(T)	(T)	0.32 *0.27* [b]	x

[a] [15] [b] [17]

The following graph, in Figure 4, combines the direct most probable absorption path from a {100} Top site evidenced just before, with NEB calculations for each O-T section of the Ni{100} supercell towards the bulk. It showed up clearly that even in terms of migration energy the surface effect was rather concentrated on the very first subsurface site. Indeed, a 0.34 eV energy was required to reach O(s-2) from O(s-1). This value was obtained for a force error lower than 0.01 eV/Å on each image. While, for H to jump from all else octahedral site to another, the energy required was of 0.40 eV. This energy is in agreement with bulk experimental data of the effective activation barrier for H given by Völkl *et al.* [42] or Fukai *et. al* [7] from 0.40 eV to 0.42 eV depending on the temperature, and more recently given by Oudriss *et al.* of 0.35 eV [60]. It also agrees with the DFT values at 0K of 0.40 eV and 0.41 eV respectively obtained by Metsue *et al*. and Wimmer *et al*. [38,61]. Finally, it appears that O(s-2) site has a H solution energy lower than in the reference bulk O site (0.11 eV), which also stands with a higher solubility in this position. Now, looking at hydrogen going back to the surface (resurfacing process), we also noticed that the required energy from T(s-0.5) to HL is extremely low, only 0.04 eV, which is coherent given the local compression between two Ni layers ($\Delta d_{12} = -2.8\%$) and the stability an HL site offers. The previous section – from O(s-1) to T(s-0.5) – was also easier for H to pass, with an activation energy of 0.32 eV. So, further than the two first Ni layers, H migration in Ni{100} already behaves like in the bulk.

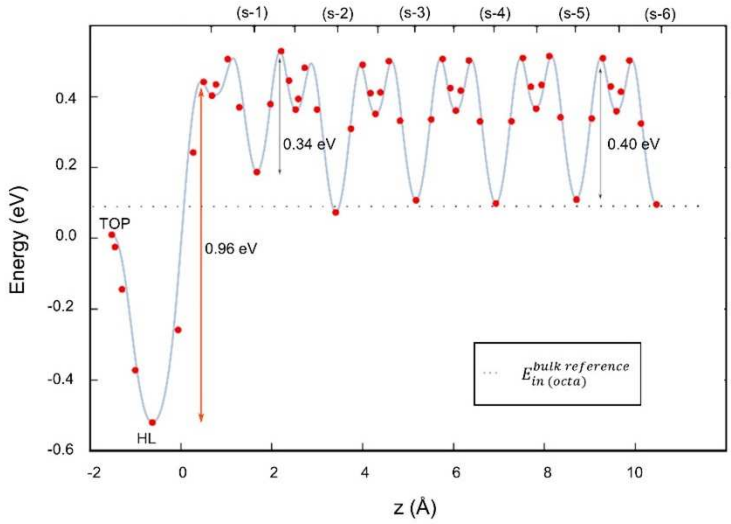

Figure 4 : Atomic H diffusion path on Ni {100} from a Top site towards the bulk, z position represents the H distance to the surface

3.2.2.Ni {110}

For {110} orientation, T sites and O sites coexist at the same z value along z which means s-1, s-2, s-3, (etc.) notation concerned both sites. Thus, as octahedral sites require less energy to be occupied, only O(s-1) were considered to calculate the possible absorption energies, and not T(s-1), as Bhatia *et al.* also did [17]. Given the reported results in Table 5, H on a {110} Top site atomic can very easily fall into any other adsorption site except from the 4F that will require H to pass through a PT site before. Moreover, as for Ni {100}, the O(s-1) site could not be reached directly. As presented in Table 5, O(s-1) can be attained either by SB, either PT site, the last path being the less energetic. In addition, PT being reachable with only 0.06 eV from SB site, or 0.15 eV from LB (migration energies in agreement with references [15] and [17]), these sites are most-likely to behave as intermediates between Top and PT sites in surface diffusion path straight to absorption. It is also remarkable that H on 4F site will have a short lifespan since moving to PT, SB or LB require no additional energy. Absorption energy from PT to O(s-1) reached 0.80 eV in our study, which also fits Bhatia *et al.*'s results. In graph represented in Figure 5, the most probable absorption path from a {110} Top surface (values from Table 5), with NEB calculations for each O-T section of our Ni{110} supercell towards the bulk. Here again, the surface relaxation effect on migration energy is limited to the first subsurface sites with a 0.38 eV necessary to reach O(s-2) from O(s-1). This value was obtained for a force error lower than 0.05 eV/Å on each image. While, for H to jump from all else octahedral site to another, the energy required was always close to 0.42 eV. This bulk energy, slightly higher than in the Ni{100} supercell case, remains coherent to experimental values. Considering resurfacing process, from O(s-1) to PT a migration energy of 0.19 eV only is required.

Table 5 : {110} Surface migration energies and absorption energies (eV) of atomic H

From \ *To*	*Top*	*PT*	*4F*	*LB*	*SB*	*O (s-1)*
Top	X	0.00	(PT)	0.01	0.00	-
PT	(SB)	x	0.23	0.15 *0.100* [a] *0.091* [b]	0.06 *0.060* [a]	0.80 *0.763* [b]
4F	(PT)	0.00	x	0.00	0.00	(PT)
LB	0.46	0.10	0.17	x	0.09	(PT)
SB	0.47	0.02	0.19	0.11	x	1.12
O (s-1)	-	0.19	(PT)	(PT)	0.54	x

[a] [15] [b] [17]

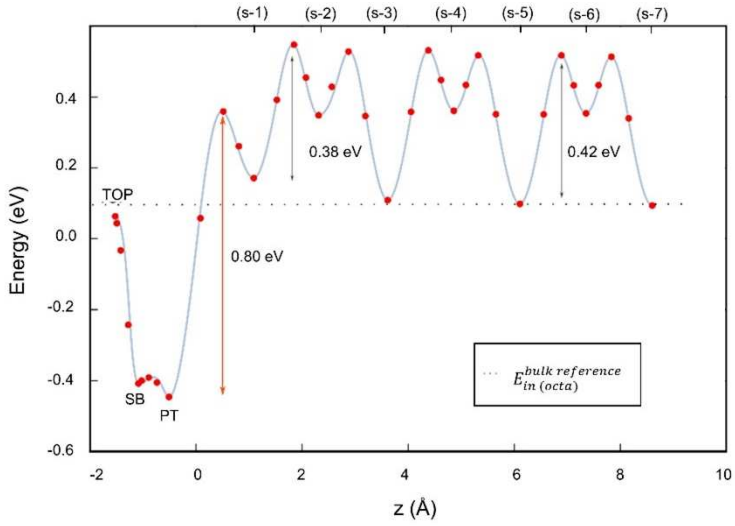

Figure 5 : Atomic H diffusion path on Ni {110} from a Top site towards the bulk, z position represents the H distance to the surface

3.2.3. Ni {111}

The diffusion profile for {111} orientation is slightly more complex and will be more detailed. In fact, for {111} Ni supercell, along z axis two T sites exist between two O positions, as presented in Table 6. Those are located at 25% and 75% of O – O distance along z. We will present mainly the path involving the second type of T site since no major differences were observed in the diffusion behavior approaching the bulk, except from the energy symmetry profile that will be discussed. We named T sites with the following notation: s-0.75, s-1.25, etc.

Table 6 : Solution energies (eV) of atomic H for the first {111} subsurface sites depending on the supercell relaxation condition The (*) corresponds to a system where H and Ni positions were fixed due to convergence troubles.

	fixed SPC volume	relaxed SPC volume	[16]
O (s-1)	0.105	0.129	0.10
T(s-0.75) under HCP	0.25 *	0.27 *	0.23
T(s-1.25) under Top	0.392	0.413	0.36
O (s-2)	0.128	0.152	0.17
T(s-1.75) on the top of a Ni atom	0.404	0.436	0.41
T(s-2.25) under a Ni atom	0.373	0.406	0.41

With summarized results in Table 7, from a Top site, an H atom can nearly spontaneously fall into a nearby FCC site for a {111} surface due to the negligible energy barrier. NEB path towards the second most stable site, HCP, seemed to make H pass through a B site before, with no activation energy required. However, when the hydrogen atom is forced to go from a Top site to B, it fell spontaneously in an FCC adsorption site first. In addition, B site coincides with FCC-HCP transition site (thus FCC-HCP energy equals to FCC-B energy, as expressed in Table 7). Also, a direct Bridge-O(s-1) forced path made the hydrogen atom go through FCC site, with an absorption energy of 0.80 eV. This value being in agreement with those reported in references [16,17]. This converged to a Top-FCC-O(s-1) path for H absorption as represented in full line in Figure 6. Another possibility is H absorption through HCP and then T(s-0.75) site followed by O(s-1) (dark blue dotted line on Figure 6). This path is nonetheless much less probable because T(s-0.75) is so unstable due to the surface proximity that we were forced to fix both Ni and H atoms positions, leading to a total force higher than our convergence criteria. Yet, H solution energy value obtained this way was very close to Greeley *et al.*'s reported value in Table 6. The resulting migration energies involving this T(s-0.75) site were nonetheless presented with less accuracy in Table 7 than other sites since the projected force perpendicular to the diffusion trajectory was between 0.1 and 0.3 eV/Å.

Once in O(s-1) position, hydrogen migration energy to reach the second octahedral site O(s-2) through T(s-1.75) is higher than in the bulk, which is the contrary of what was observed on Ni {100} and Ni {110} surfaces. While, to reach the third O site the migration energy reached 0.43 eV, before stabilizing around 0.45 meV, drawing an easier jump for H before behaving as in the bulk (Figure 6). As also reported by Greeley *et al.*, another possible path for hydrogen in O(s-1) is to reach a T(s-1.25) site before O(s-2). However our NEB calculations O(s-1) - T(s-1.25) never converged within our force criteria and the k-mesh density imposed, meanwhile the T(s-1.25) - O(s-2) jump did, involving a 0.23 eV activation energy. This convergence trouble was observed similarly for O(s-2) - T(s-2.25) and O(s-3) - T(s-3.25) but not for the others. We decided nonetheless to represent the alternative the path (refer to the dashed

line in Figure 6) with the results whose error was closest to the criterion to discuss about global the energetic asymmetry observed for both paths, which was not the case for the two others orientations investigated here. Greeley also mentioned this asymmetry with a migration energy of 0.52 eV and 0.26 eV for respectively O(s-1) - T(s-1.75) and O(s-1) - T(s-1.25) paths.

Table 7 : {111} Surface migration energies and absorption energies (eV) of atomic H.

From \ *To*	*Top*	*FCC*	*HCP*	*Bridge*	*T (s-0.75)*	*O (s-1)*	*T (s-1.75)*
Top	X	0.00	(B)	(FCC)	-	(FCC)	-
FCC	0.57	x	(B)	0.15 *0.150* [a]	-	0.80 *0.837* [b] *0.88* [c]	-
HCP	(B)	(B)	x	0.13 *0.12* [b]	0.8	(T)	-
Bridge	-	0.00	0.00	x	-	(FCC)	-
T (s-0.75)	-	-	0.0	-	x	0.2	-
O (s-1)	(FCC)	0.14 *0.17* [c]	(T)	(FCC)	0.32	x	0.51 *0.52* [c] *1.12* [b]
T (s-1.75)	-	-	-	-	-	0.21 *0.21* [c]	x

[a] [15] [b] [17] [c] [16]

This asymmetry is due to the fact that for this orientation, for each O-O jump one O-T section is exactly along the $[\bar{1}1\bar{1}]$ that holds the surface, and the other one is held by the $[\bar{1}\bar{1}\bar{1}]$ makes an angle of 30° from the horizontal. The second type of jump is nearly a z-constant jump and involves a lower migration energy, while the first is directly along the symmetry break, which involves logically a higher energy barrier. We assume that larger supercells along x and y axes might tend to reduce this asymmetry, at least reaching the center of the supercell. The fact that for this orientation our H bulk migration energy is higher is clearly related. In fact, by averaging the two saddle points energies involved in the last jump that reaches the supercell center, we obtain a mean energy barrier of 0.42 eV, which is in better agreement with reference values [38,61]. Using this same reasoning by meaning saddle point energies for the first and second O-O jumps, the respective migration energies became then 0.46 eV and 0.39 eV. About the resurfacing process, a 0.137 eV barrier energy is involved here for H to get extracted from the Ni slab, which is in between {110} and {111} surfaces ones. This value is close to the Case 2 and 3 values (0.16 eV) of Sha *et al.*'s study, but far from the experimental ones that are rather in the range of 0.35-0.45 eV [39,62] due to adsorbates at the surface. This observation leads to the conclusion that not

allowing the relaxation favors results closer to the experiments values [39], at least for this {111} orientation.

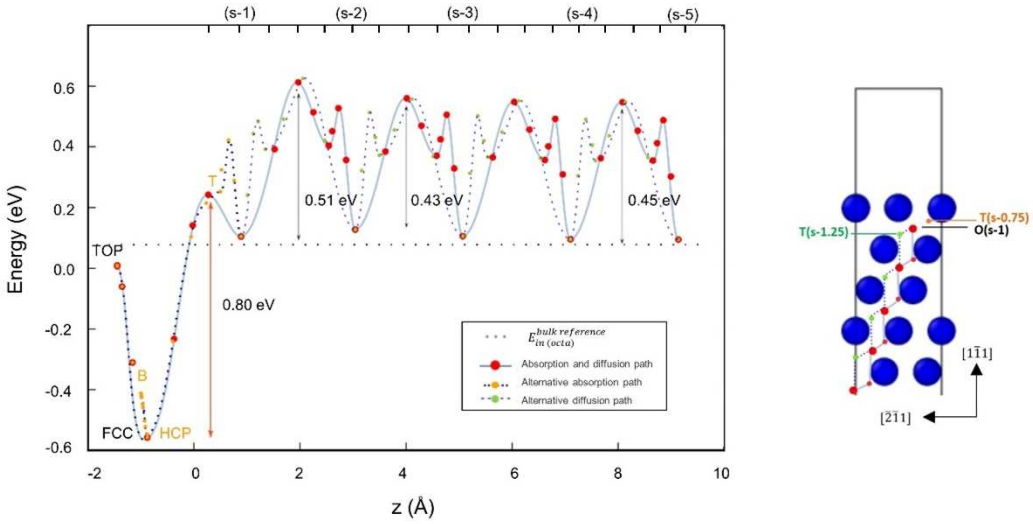

Figure 6 : Atomic H diffusion paths on Ni {111} from a Top site towards the bulk, with the corresponding profiles in the half {111} supercell.

3.3. Orientation impact on subsurface diffusion towards the bulk

Thanks to the energy barriers highlighted in the previous section, we then evaluated numerically and at 0K the most probable path for hydrogen to reach the bulk during experimental cathodic H-charging tests (OPD-H mechanism), all this from different crystallographic orientations. It appeared that from the initial Top site position, hydrogen will necessarily occupy a higher symmetry site before reaching the first O subsurface site (s-1). Top adsorbed H on surface {110} presents the particularity to rather occupy a SB (or LB for other authors [15,17]) position before reaching the PT site. However, the migration energy values obtained in this research are valid in the scope of the investigated coverage (1/4). That is to say, other adsorption sites could also be occupied in between or instead for higher coverages, and absorption energies should be impacted. In addition, H migration energies might be more favorable for subsurface diffusion (constant z position), as evidenced for O-T sections in {111} orientation, which was not at really fully studied in this work, but this point would be complementary to the idea we will now develop.

Based on Wert and Zener application of Eyring's transition state theory [63] to interstitial diffusion in metals, the diffusion coefficient can be written within the random walk theory framework as [38,64] :

$$D = n\beta d^2\Gamma \tag{9}$$

with n the number of nearest-neighbor octahedral sites for the hydrogen interstitial atom (12 for fcc metals), β corresponds to the probability that a jump to a nearest octahedral site is in the considered direction of diffusion (*i.e.* perpendicular to the surface and towards the bulk here), and finally d is the

jump distance projection in the diffusion direction. Γ is defined as the jump rate between two nearest-neighbor sites and equals the reverse of the mean time-of-stay evoked by Wert and Zener. Moreover, for all fcc metals, we have whichever the diffusion direction considered : $n\beta d^2 = a^2$. Where a is the lattice parameter, the βd^2 factor always leading to $a^2/12$. This equality has been verified for the 3 surfaces studied in this work for H in every octahedral position.

For low temperature, the jump rate can be written [38]:

$$\Gamma = \frac{kT}{h}\, e^{-\frac{\left(E_{mig}+\Delta E_{ZP}\right)_{TS-O}}{kT}} \tag{10}$$

With E_{mig} the migration energy barriers required to go beyond the saddle points (TS : transition sites) we calculated, and ΔE_{ZP} corresponds to the ZPE correction to this energy barrier. Though we did not calculate it for each investigated barrier in this study, Wimmer *et al.* found a ZPE correction of 0.038 eV for the bulk nickel, while Metsue *et al.* found a slightly higher value of 0.05 eV [38,61]. For H in {111} subsurface nickel Greeley *et al.* found a ZPE correction to the migration energy barrier around 0.03 eV [16]. Yet, conversely to the reported values that were obtained for different supercells, we worked in this study with the same H concentrations and k-mesh for each orientation. Thus, we decided to make the rough approximation that the correction would be the same for an H atom in a supercell subsurface site and in the corresponding oriented bulk, given the very slight energy barrier corrections highlighted.

In the light of these elements, we could finally establish for each orientation the hydrogen diffusion coefficient ratio between the local subsurface (sub) site occupied and the bulk:

$$\frac{D_{sub}}{D_{bulk}} = \frac{\Gamma_{sub}}{\Gamma_{bulk}} \cong e^{\frac{-E_{mig}^{sub}+E_{migr}^{bulk}}{kT}} \tag{11}$$

In order to assess the local ratio for the three studied crystallographic orientations, we used T=300K assuming that at the ambient diffusion process remain close to those at 0K (as far as tunnel effect is not of concern here). Since for the three orientations only the (two) first H-octahedral host sites require a migration energy significantly different from a bulk-like site, the ratio was only established from these positions of interest.

Table 8 : Local acceleration of H diffusion. For {111} orientation, the two first subsurface atomic layers present different migration energy to the bulk, which explains the larger spatial extension for this orientation and the two diffusion coefficient ratio values. The values in brackets for {111} orientation refer to the corresponding mean migration energies by erasing the TS sites' energy asymmetry.

Crystallographic orientation	*Spatial extension of diffusion acceleration*	E_{mig}^{sub}	$\frac{D_{sub}}{D_{bulk}}$
{100}	0.4 nm	0.34 eV	10.2
{110}	0.4 nm	0.38 eV	4.7
{111}	0.6 nm	0.51 eV (0.46) 0.40 eV (0.39)	0.1 (0.2) 2.2 (3.2)

By Table 8, if we can certainly talk of local acceleration for {100} and {110} surface, the phenomenon is less clear for the most compact surface. Indeed, about {111} orientation, it appears that we have first a deceleration step with $D_{sub} \approx D_{bulk}/10$ before having a modest acceleration. Moreover, the acceleration close to the surface appears to be the highest for {100} orientation by far, followed by {110} and then {111}. In a former experimental study, Li et al. also highlighted such H anisotropy of diffusion in bulk nickel but in reverse order [65]. However, when a coverage of 25% is considered low, 3D-concentrations of 1H/40Ni ({111}), 1H/52Ni ({110}) or 1H/60Ni ({110}) are huge. The higher the concentration is, the more H atoms of adjacent cells have to overcome transition sites simultaneously, which increases the corresponding energy barriers and affects the local diffusion coefficient. Moreover, once H penetrated the slab, we did not maintain H atoms positioned on adsorption sites, meanwhile hydrogen adsorbed atoms are constantly present during electrochemical charging. Yet, this adsorption layer has an effect on Ni relaxed positions, and then the local geometry of host octahedral sites for instance, but also on the global host matrix geometry, which might significantly impact both migration and insertion energies as well. Hence, the perfect surfaces are not directly comparable to these experimental results [65]. From Table 8 one can also conclude that the local diffusion acceleration noticed here is very limited in terms of spatial extension (only two or three atomic layers), which is much lower than distances investigated experimentally [66].

Further studies at finite temperature (starting with ZPE corrections) would be impactful to see how thermal vibrations affect such subsurface anisotropy. In addition, higher surface coverage and lower slab concentration would be of great interest in order to identify their respective effect, as to add punctual defects like vacancies close to the surfaces as started recently Metsue *et al.* [61]. Such defects, as well as terraces and kinks would make our model tend to get closer to real materials and modify the activation barriers [17,67]. However, larger supercells being required, such studies might need a larger scale study, even a multiscale one. Diffusion at constant z distance to the surface would also be valuable, even if the H concentration gradient will favor a diffusion process toward the bulk.

4. Surface impact on local H-solubility

After considering H-diffusivity close to oriented surfaces we desired to correlate the H solubility ratio in a given site to its local geometry. Once more, our sites of interest are defined by their relative distance to the oriented surface {100}, {110} and {111}. However, H incorporation energies used to calculate local solubility hide two energetic phenomena: the displacement field of all Ni atoms (the initial O sites deformation) due to the surface, and their propensity to accommodate to host an interstitial atom that might be higher than in the bulk thanks to the vacuum proximity. Yet, before assessing the sites deformation matrix due to H incorporation, we first assessed their primary deformation due to the surface itself, as described in step 1 in the method section. We focused here on the displacement field

of the 6 Ni atoms that define an octahedron, not those of the surroundings. Such approach will have no major impact on the results of this first step, but it will in the second step when hydrogen will be incorporated. Disregard self-stress induced by second (even third) Ni neighbors will underestimate the real effective energy that affects H in such positions. In order to permit clearer vision of the O sites' tilt depending on the surface crystallographic orientation, the specific O (s-1) sites for each {hkl} slab were represented in Figure 7, both in terms of Ni atomic positions and Voronoï's volume. The <100> family vectors that define the common base used to calculate the deformation matrix are also represented in each supercell to ease one's space orientation.

4.1. Surface induced displacement field and local elastic energy

Following the different steps mentioned in method section we obtained hydrostatic and shear strains, respectively ϵ_m and ϵ_{eq}^d, and the corresponding elastic energies for each O site. Since $\epsilon_m = \frac{1}{3}\frac{\Delta V}{V_{O_{bulk}}} = \frac{1}{3}\frac{V_O - V_{O_{bulk}}}{V_{O_{bulk}}}$, the local volume dilatation were calculated using the reference value $V_{O_{bulk}}$= 5.46Å^3 for a vacant site. Figure 8a reveals that all sites except from (s-2) one for {110} orientation were in compression, and more specifically the (s-1) site for {110} orientation. The local (s-2) dilatation for {110} orientation was already mentioned in the significant positive Δd_{23} value (Table 2). This site is also one of the most deformed with (s-1) one of the same orientation (Figure 2) and (s-2) of {100} slab. However the ratios of each contributions (hydrostatic and distortional) were not represented here since internal elastic are negligible for sites deeper than 2 Å with a value lower 0.35 meV, as shown in Figure 8b. This local energy convergence towards the bulk reference value of 0 eV with an error inferior to 1meV confirms the validity of our energetic hypothesis that supercell centers reach bulk energetic properties, even if surface still has an effect in terms of initial available volume for H.

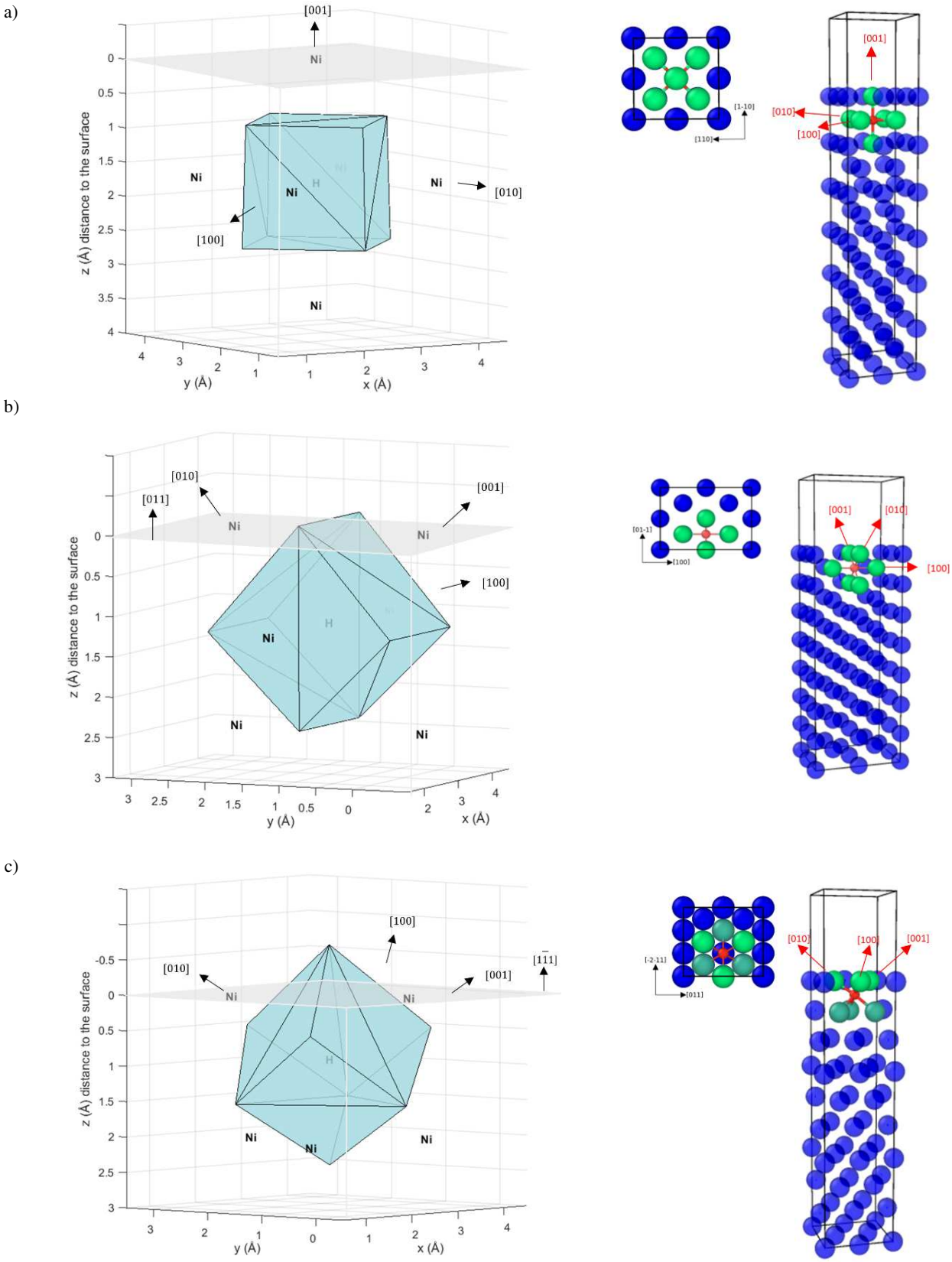

Figure 7 : Schematic and oriented representation of a hydrogen atom positioned in (s-1) octahedral sites in a) {100}, b) {110} and c) {111} supercells. On the left : the volume geometry of each site obtained by Voronoï's method, with both the (x,y,z) positions of Ni and H atoms in the supercells, and the <100> vectors family that define the common base used to calculate the deformation matrix. On the right, the involved Ni (green) and H (red) atoms involved in a (s-1) site are hig hlighted in each supercell.

Besides, a parallel can be drawn between these compression values, all between -0.045 and -0.005, and those observed close to a mono-vacancy in bulk nickel [44] (between -0.037 and -0.005 for DFT calculated values). Surface effect in terms of induced hydrostatic strain has the same order of magnitude as a vacancy [44].The same remark applies to its spatial extent since the displacement field becomes negligible beyond a 6 Å distance to the vacancy core, which coincides with the scope of diffusion acceleration. In addition, we noticed that between 1 to 3 Å we obtained the same classification between crystallographic orientations as Metsue *et al.* got for sites along these directions from the vacancy [44].

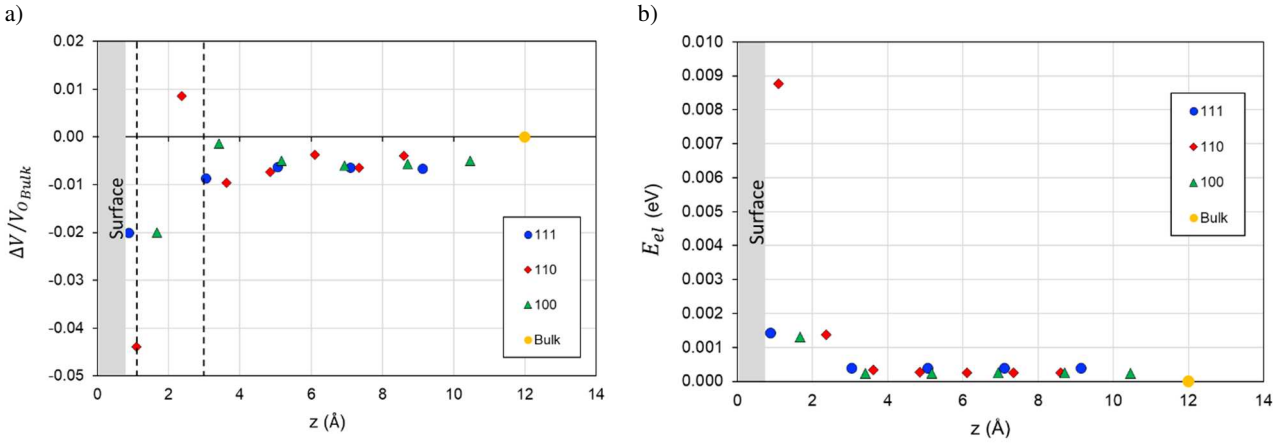

Figure 8: a) Local volume dilatation of O sites depending on their z-distance to {100}, {110} and {111} surfaces and b) associated internal elastic energies, compared to the unstressed bulk reference (O site in relaxed conventional cell).

With this first step we identified the initial state of each possible O sites, with an internal elastic energy for {110} (s-1) around 10 times higher than others, due to the high compression. Other (s-1) sites are also the most impacted, but five times less, and the {110} (s-2) site might be able to host an H atom more easily than the reference bulk site. We took then these sites as their reference and introduced one hydrogen atom inside.

4.2. Hydrogen induced displacement field and local elastic energy

In this second part we calculated the final volume of octahedral sites, their relative variation in comparison with their initial state (without H), their possible deviation to cubic shape and the extra energy necessary to furnish locally for hydrogen to occupy these investigated sites. First, as presented in Figure 9a the final volume of each octahedral site with hydrogen V_H depending on the depth presents the same profile as the local dilatation profile observed in step 1. Indeed, the ratio $V_H/V_O \approx 1.07$ was respected for most sites, this explains the linear behavior of Figure 9b. However, on this last one, we notice that for {111} and {110} (s-1) sites, the ratio was much higher. This means that, from their own initial volume V_O, their dilatation $(V_H\text{-}V_O)/V_O$ was much higher than in other sites, as suggested in the prelude of this part. The energy of these sites is then logically higher than for H occupying other positions (Figure 9c). Thus, in a local point of view, these two (s-1) sites are, at the concerned octahedral

site scale, the most energetic ones for a hydrogen atom. We also notice that for the great majority of O sites, in the scope of elastic isotropy, hydrostatic contributions highly exceeded the distortional ones (Figure 9d). Only the two first subsurface sites of {110} oriented surface can't be fully represented only by their volume change. Concerning {100} orientation, the V_H/V_O ratio was perfectly observed for each site. It is also remarkable that O(s-2) {100} position presents the closest volume to the 5.81 Å^3 value in the relaxed bulk ($V_{H\,bulk}$). Finally, even though at the center of each supercell the V_H volume is 0.02 Å^3 below the bulk reference value, all internal stress energies converge the H-internal bulk elastic energy within less than 1 meV. This confirms again that the supercells center behaves like the bulk in terms of energy. However, the local elastic energy excess due to H incorporation obtained for the bulk is barely 12% of the global H-incorporation energy value. In addition, this local energy excess in {111} (s-1) site didn't meet the global incorporation energy evolution for this orientation. This highlights the importance of longer-range strain field exploration, not just the first 6 Ni neighboring atoms composing the octahedron.

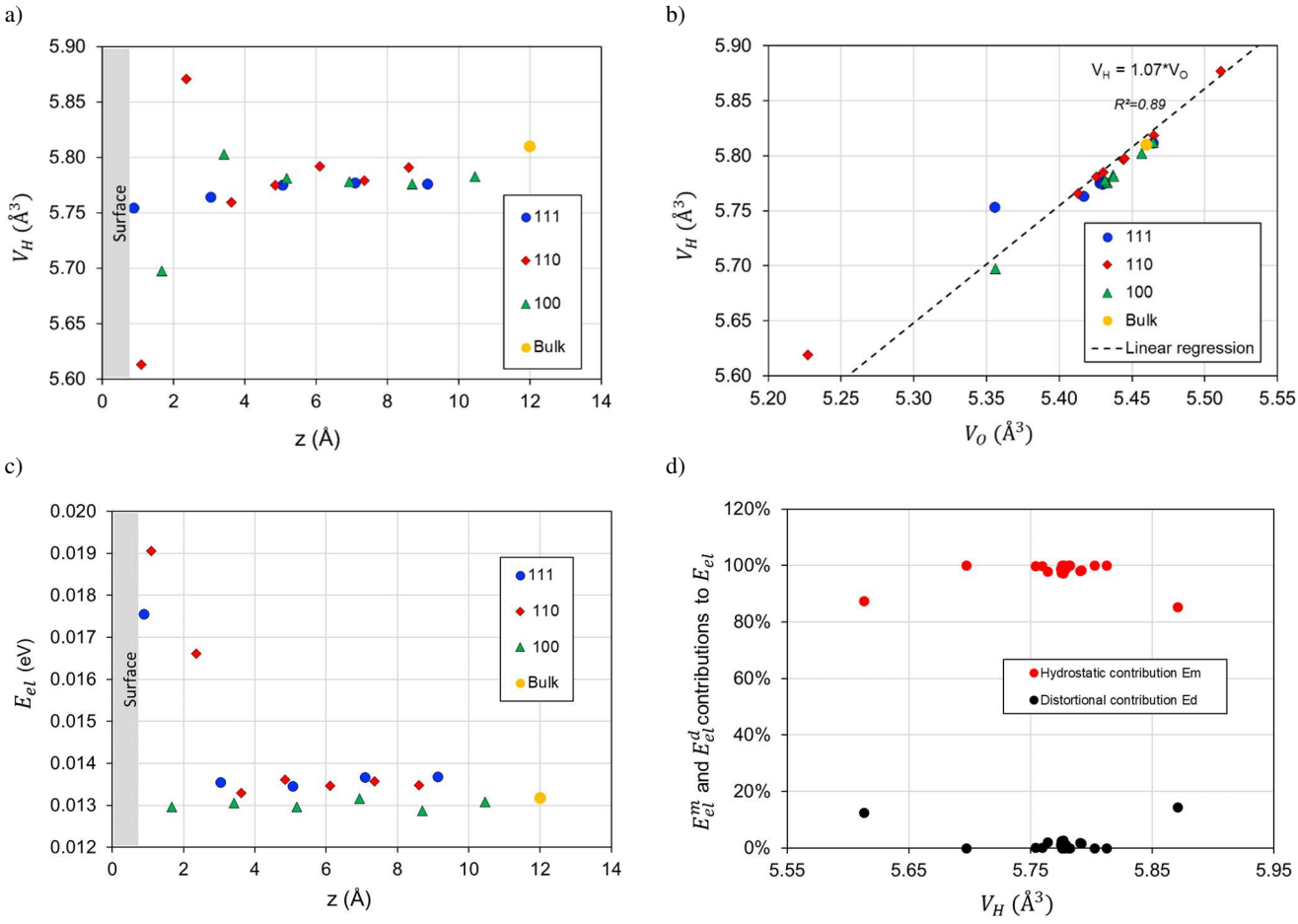

Figure 9 : a) Octahedral sites volume with hydrogen depending on their distance to the surface. b) Evolution between of the octahedral sites volume with hydrogen compared to the corresponding empty volume. c) Local elastic energy felt by a hydrogen atom depending on the host O-site distance to the surface. d) Global distortional and hydrostatic contributions to local elastic energy depending on the site volume

4.3. From local geometry to long range energy

Given the difference of magnitude between H incorporation energy (E_{in}) and the local elastic energy (E_{el}), we decided to express H local solubility with the local volume change directly, since it appeared to be the dominating effect. On one hand, atomic hydrogen solubility s(z,T) in each octahedral site at a given z position and temperature T is linked to the associated incorporation energy E_{in} by Sieverts' law (12):

$$s(z,T) = \sqrt{P}\exp\left(\frac{-E_{in}(z,T)}{k_bT}\right) \quad (12)$$

This relation enabled us to assess for each site the solubility ratio at ambient temperature (300K) in comparison to the bulk octahedral solubility $s_o(T)$ using the following equation (13):

$$\frac{s(z,T)}{s_o(T)} = \exp\left(\frac{E_{in_{bulk}}(T) - E_{in}(z,T)}{k_bT}\right) \quad (13)$$

However, taking into account the model of the hydrogen chemical potential modified by the action of an hydrostatic stress field $\sigma_m(z,T)$, the local solubility ratio can also be expressed as follows [31,68] :

$$\frac{s(z,T)}{s_o(T)} = \exp\left(\frac{\overline{v_H}\,\sigma_m(z,T)}{k_bT}\right) = \exp\left(\frac{\overline{v_H}\,B}{k_bT}\frac{\Delta V}{V}\right) \quad (14)$$

Where $\overline{v_H}$ is the partial molar volume of hydrogen, representing the global volume dilatation when one H atom is introduced in a relaxed bulk supercell (*i.e.* unstressed). In this last case, $\frac{\Delta V}{V} = \frac{V_H - V_{H_{bulk}}}{V_{H_{bulk}}}$ represents here the volume dilatation of a site with an hydrogen atom inside V_H, compared to the reference volume of an O site occupied ($V_{H_{bulk}}$ =5.81 Å^3) in an unstressed crystal.

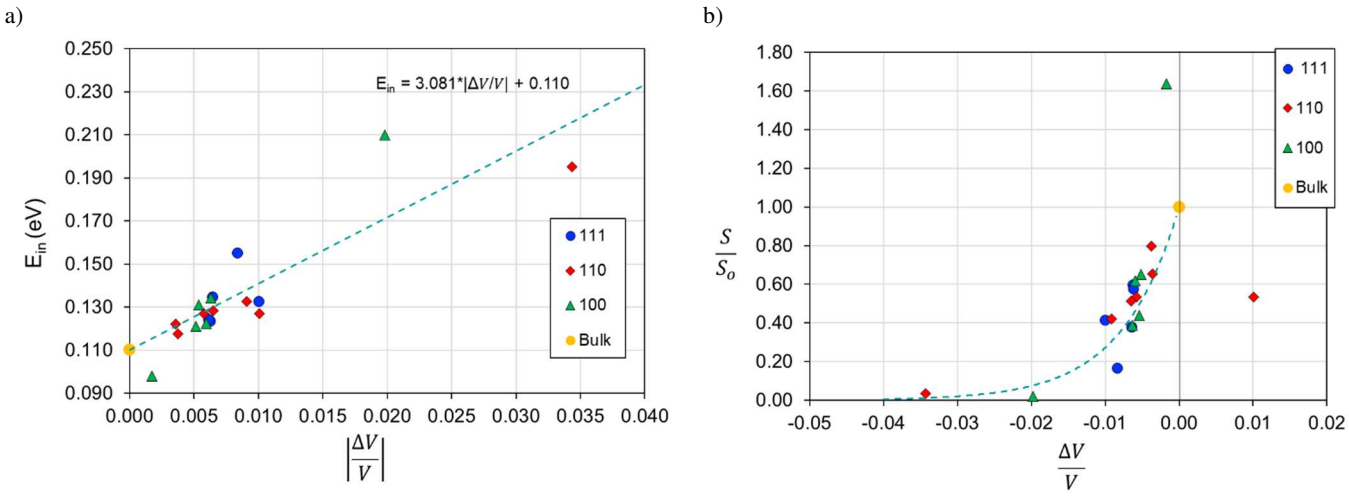

Figure 10 : a) H insertion energy depending on the local volume dilatation. b) The corollary representation using the solubility ratio.

As illustrates Figure 10a, the global insertion energy (E_{in}) was plotted as a function of the absolute value of local volume dilatation with respect to the bulk reference with H, as previously did Zhou *et al*. and Li *et al*. at grain boundaries surroundings [25,46]. Regardless the orientation, the mean slope obtained accordingly was of 3.081 eV. The equivalent representation in terms of solubility ratio calculated with equation (13), is represented beside (Figure 10b). Using (14), and since for the three oriented bulk slabs we obtained $\overline{v_H} = 2.25 \pm 0.04\ \text{Å}^3/at$, we identified a mean Bulk modulus value B = 219 GPa. If the partial molar volume is in agreement with previous DFT studies $\overline{v_H} = 2.31\ \text{Å}^3/at$ in Nazarov *et al.* [69], or $2.22\ \text{Å}^3/at$ Metsue *et al.* [32], the Bulk Modulus rather tends to be between 180 and 204 GPa [7,31,70], even if 221 GPa value for nickel was reported by You *et al* [71]. Thus, even by making the rude linear approximation without considering crystallographic orientation, we were relatively well abled to correlate the local volume change with the local solubility, these values referring respectively to long-range and short-range energies. Moreover, such linear behavior had already been discussed by Hallil *et al.* near Σ3 grain boundaries for least dilated sites [43] since the distortion contribution was minor. It should however be noted that, in their study, the investigated sites were more favorable compared to unstressed bulk octahedral site, conversely to this present study where sites are more energetic. Moreover, in the present work, only the first Ni atoms neighbors' effect on H host sites was taken into account. Meanwhile, in [43] the second and third Ni site-neighbors impact on local stress field was counted on the GB case, making local elastic energies values directly comparable with segregation energies.

Now, looking at each orientation separately, Figure 10a revealed a clear linear relation for {100} and {110} sites. Such linearity was more difficult to observe for {111} orientation, for which the corresponding O sites alternatively seemed to fit to {100} and {110} linear regressions, which might suggests an intermediate behavior. The slope ratio {100}/{110} after forcing the intercept of 0.110 eV value was around 1.8. This slope variation significance reveals that surfaces might present different elastic constants from the bulk, which wasn't evoked so far. Yet, as showed Shenoy, Bulk modulus are very different depending on surface orientation, and present the following order for nickel B(001)>B(111)>B(110) [72], with a negative value for the last one though. This last element very interesting as regards the slope evolutions highlighted in Figure 10a since we obtained the same ranking between the three orientations, suggesting a Bulk modulus different from the bulk value in subsurface areas too.

In the end, making the assumption of isotropic elasticity to calculate elastic energies, we highlighted low distortional contributions for the majority of O sites (Figure 9d), these could thus mostly be described by their volume change. This approximation made sense given the coherent global Bulk modulus we obtained of 219 GPa with this purely hydrostatic description. Nevertheless, we must note that in particular for one {110} site (s-2), whose ΔV/V > 0, this description doesn't fit. As a reminder, this site was one of the two whose calculated shear contribution (E_{el}^{d}) was the closest to 20% (Figure

9b). Moreover, as we used isotropic elasticity in order to assess both hydrostatic and shear parts to elastic energy, we actually might have lowered this last one's impact since the displacements measured were not isotropic, mostly due to the symmetry break along *z*. Then, going back to the initial description of the hydrogen chemical potential μ_H in absence of external stress that includes all σ_{ij} stress components would be valuable to have a more accurate description of local hydrogen solubility [73,74]:

$$\mu_H = \mu_O + k_B T \ln\left(\frac{C_H}{1 - C_H}\right) - \Omega \sigma_{ij} \epsilon_{ij} \quad (15)$$

Where C_H is the hydrogen concentration and Ω the atomic volume. Indeed, in other systems some authors recently pointed out the importance of shear stress contribution in trapping processes and in hydrogen diffusivity, leading to anisotropic behavior [49,65,75]. Moreover, Dyre *et al.* demonstrated that shear elastic energy predominates far from punctual defects [76], which underlines the importance to assess the displacement fields beyond the first Ni atoms that compose octahedral sites to link directly the elastic energy to global H incorporation energy in one specific site.

5. Conclusions

The present work was articulated in two parts. First, diffusion profiles for H from Top adsorption sites have been drawn. Top sites being occupied by atomic H during electrochemically charging tests (OPD-H), these profiles confirmed first that the hydrogen will fall first in a more stable ones (closer to the surface) before reaching first octahedral sites, given the distance is has to browse. These profiles also underlined that subsurface migration barriers are different from the bulk and vary depending on the crystallographic orientation, revealing a local anisotropic diffusive behavior. In terms of diffusion coefficient ratios, a neat acceleration appeared for H in extreme {100} subsurface in comparison with the bulk. A moderate acceleration was also evidenced for H in {110} subsurface. Meanwhile, the {111} orientation seemed to present too steps, with a diffusion deceleration before showing a slight local acceleration. The fact {111} surface is the most stable one may explain the limited effects observed at its surroundings in terms of energy barriers. However, we noted that globally the spatial extent of the evoked anisotropy remained limited to the two first atomic layers under the three investigated surfaces. Nevertheless, our calculations did not take into account thermal nor electronic vibrations contributions to migration energy barriers, which might change the observed phenomena. Adding these contributions to this description would be significant, as it has already been done near vacancy core [61]. Moreover, the absence of surface defects in our model as well as the high hydrogen concentration in our cells make our results difficult to compare with previous experimental ones.

Second, we focused on octahedral sites successively occupied in the diffusion process to identify the geometry change due to surface relaxation and to H incorporation. Once more, both impacts were limited to the very first sites under the considered oriented surfaces. The local contraction involved by surface relaxation had the same magnitude as vacancy effect on neighboring O sites. Moreover, except for some

{110} O sites, the shear strain contribution on local elastic energy due to H incorporation (involving a geometry change) appeared to be negligible in comparison with the hydrostatic contribution (referring to a volume change). However, to calculate these elastic energies we needed to make the approximation of isotropic elasticity. Such an assumption then tends to underestimate the real deviating contribution of the calculated energy. Besides, by limiting our O sites descriptions to the 6 Ni atoms that define it, the elastic energy calculated from the displacement field was much lower than the associated H incorporation energy that hides both long range and short range effects. Yet, as distortion contributions were evidenced to be higher far from punctual defects, a larger analysis on more Ni displacement field due to H incorporation would be necessary [76]. Nonetheless, a good correlation appeared between H local solubility and the volume available. Looking at each orientation's behavior, this last observation also enhanced that subsurface elastic constants could vary depending on the orientation considered, which echoes similar observation for surface Bulk modulus [72]. Finally, stepped surfaces presenting punctual defects would be relevant to investigate to identify their combined effect on local solubility and to get closer to real surfaces behavior. Also, modelling slip bands appearance on these 3 surfaces would enable to identify the first step interactions between hydrogen and mechanically solicited materials, as it happens in industrial processes and more generally in everyday life.

Acknowledgments

The authors would like to acknowledge the funding from French Research National Agency (ANR) through the CRACKHINIT project (Contract ANR-17-CE08-0023-01).

The authors acknowledge Dr. Guillaume Hachet for his contribution to improve the manuscript.

Data availability

The raw/processed data that support the findings of this work are available upon reasonable request.

References

[1] S. Lynch, Hydrogen embrittlement phenomena and mechanisms, Corros. Rev. 30 (2012). https://doi.org/10.1515/corrrev-2012-0502.

[2] R.P. Gangloff, B.P. Somerday, eds., Mechanisms, modelling and future developments, Woodhead Publ, Oxford, 2012.

[3] I.M. Robertson, P. Sofronis, A. Nagao, M.L. Martin, S. Wang, D.W. Gross, K.E. Nygren, Hydrogen Embrittlement Understood, Metall. Mater. Trans. A. 46 (2015) 2323–2341. https://doi.org/10.1007/s11661-015-2836-1.

[4] M. Nagumo, Fundamentals of Hydrogen Embrittlement, Springer Singapore, Singapore, 2016. https://doi.org/10.1007/978-981-10-0161-1.

[5] A.T. Paxton, A.P. Sutton, M.W. Finnis, The challenges of hydrogen and metals, Philos. Trans. R. Soc. Math. Phys. Eng. Sci. 375 (2017) 20170198. https://doi.org/10.1098/rsta.2017.0198.

[6] R. Kirchheim, Hydrogen solubility and diffusivity in defective and amorphous metals, Prog. Mater. Sci. 32 (1988) 261–325. https://doi.org/10.1016/0079-6425(88)90010-2.

[7] Y. Fukai, The Metal-Hydrogen System : Basic Bulk Properties, Springer-Verlag, Berlin, 2006.

[8] J. Greeley, M. Mavrikakis, Surface and Subsurface Hydrogen: Adsorption Properties on Transition Metals and Near-Surface Alloys, J. Phys. Chem. B. 109 (2005) 3460–3471. https://doi.org/10.1021/jp046540q.

[9] T. Mitsui, M.K. Rose, E. Fomin, D.F. Ogletree, M. Salmeron, Dissociative hydrogen adsorption on palladium requires aggregates of three or more vacancies, Nature. 422 (2003) 705–707. https://doi.org/10.1038/nature01557.

[10] G. Jerkiewicz, Hydrogen sorption at/in electrodes, Prog. Surf. Sci. 57 (1998) 137–186. https://doi.org/10.1016/S0079-6816(98)00015-X.

[11] S. Sakong, A. Groß, Dissociative adsorption of hydrogen on strained Cu surfaces, Surf. Sci. 525 (2003) 107–118. https://doi.org/10.1016/S0039-6028(02)02550-5.

[12] M. Pozzo, D. Alfè, Hydrogen dissociation and diffusion on transition metal (=Ti, Zr, V, Fe, Ru, Co, Rh, Ni, Pd, Cu, Ag)-doped Mg(0001) surfaces, Int. J. Hydrog. Energy. 34 (2009) 1922–1930. https://doi.org/10.1016/j.ijhydene.2008.11.109.

[13] M.S. Hofman, D.Z. Wang, Y. Yang, B.E. Koel, Interactions of incident H atoms with metal surfaces, Surf. Sci. Rep. 73 (2018) 153–189. https://doi.org/10.1016/j.surfrep.2018.06.001.

[14] K. Christmann, O. Schober, G. Ertl, M. Neumann, Adsorption of hydrogen on nickel single crystal surfaces, J. Chem. Phys. 60 (1974) 4528–4540. https://doi.org/10.1063/1.1680935.

[15] G. Kresse, J. Hafner, First-principles study of the adsorption of atomic H on Ni (111), (100) and (110), Surf. Sci. 459 (2000) 287–302. https://doi.org/10.1016/S0039-6028(00)00457-X.

[16] J. Greeley, M. Mavrikakis, A first-principles study of surface and subsurface H on and in Ni(111): diffusional properties and coverage-dependent behavior, Surf. Sci. 540 (2003) 215–229. https://doi.org/10.1016/S0039-6028(03)00790-8.

[17] B. Bhatia, D.S. Sholl, Chemisorption and diffusion of hydrogen on surface and subsurface sites of flat and stepped nickel surfaces, J. Chem. Phys. 122 (2005) 204707. https://doi.org/10.1063/1.1902943.

[18] Y.Y. Huang, Y.C. Zhou, Y. Pan, Effects of hydrogen adsorption on the surface-energy anisotropy of nickel, Phys. B Condens. Matter. 405 (2010) 1335–1338. https://doi.org/10.1016/j.physb.2009.11.082.

[19] H. El Alami, J. Creus, R. Sabot, X. Feaugas, Influence of microstructural heterogeneities on hydrogen evolution at different scales, Adv. Mater. Sci. 7 (2007) 140–146.

[20] K.J. Maynard, A.D. Johnson, S.P. Daley, S.T. Ceyer, A new mechanism for absorption: collision-induced absorption, Faraday Discuss. Chem. Soc. 91 (1991) 437. https://doi.org/10.1039/dc9919100437.

[21] B.E. Conway, G. Jerkiewicz, Relation of energies and coverages of underpotential and overpotential deposited H at Pt and other metals to the 'volcano curve' for cathodic H2 evolution kinetics, Electrochimica Acta. 45 (2000) 4075–4083. https://doi.org/10.1016/S0013-4686(00)00523-5.

[22] E. Protopopoff, P. Marcus, Surface Effects on Hydrogen Entry into Metals, in: P. Marcus (Ed.), Corros. Mech. Theory Pract., Second Edition, CRC Press, 2002: pp. 53–96. https://doi.org/10.1201/9780203909188.ch3.

[23] R.J. Nichols, A. Bewick, Spectroscopic identification of the adsorbed intermediate in hydrogen evolution on platinum, J. Electroanal. Chem. Interfacial Electrochem. 243 (1988) 445–453. https://doi.org/10.1016/0022-0728(88)80047-0.

[24] Bockris, The equivalent pressure of molecular hydrogen in cavities within metals in terms of the overpotential developed during the evolution of hydrogen, (1971). https://doi.org/10.1016/0013-4686(71)85027-2Get.

[25] J. Li, The contribution of the grain boundary engineering to the problem of intergranular hydrogen embrittlement, La Rochelle University, 2017.

[26] G. Hachet, J. Li, A.M. Hallil, A. Metsue, A. Oudriss, J. Bouhattate, X. Feaugas, A multi-scale analysis of the different interactions between defects and hydrogen: A review on the contribution of the elastic fields, Eng. Fract. Mech. 218 (2019) 106621. https://doi.org/10.1016/j.engfracmech.2019.106621.

[27] P. Hohenberg, W. Kohn, Inhomogeneous Electron Gas, Phys. Rev. 136 (1964) B864–B871. https://doi.org/10.1103/PhysRev.136.B864.

[28] W. Kohn, L.J. Sham, Self-Consistent Equations Including Exchange and Correlation Effects, Phys. Rev. 140 (1965) A1133–A1138. https://doi.org/10.1103/PhysRev.140.A1133.

[29] P. Giannozzi, S. Baroni, N. Bonini, M. Calandra, R. Car, C. Cavazzoni, D. Ceresoli, G.L. Chiarotti, M. Cococcioni, I. Dabo, A. Dal Corso, S. de Gironcoli, S. Fabris, G. Fratesi, R. Gebauer, U. Gerstmann, C. Gougoussis, A. Kokalj, M. Lazzeri, L. Martin-Samos, N. Marzari, F. Mauri, R. Mazzarello, S. Paolini, A. Pasquarello, L. Paulatto, C. Sbraccia, S. Scandolo, G. Sclauzero, A.P. Seitsonen, A. Smogunov, P. Umari, R.M. Wentzcovitch, QUANTUM ESPRESSO: a modular and open-source software project for quantum simulations of materials, J. Phys. Condens. Matter. 21 (2009) 395502. https://doi.org/10.1088/0953-8984/21/39/395502.

[30] P.E. Blöchl, Projector augmented-wave method, Phys. Rev. B. 50 (1994) 17953–17979. https://doi.org/10.1103/PhysRevB.50.17953.

[31] A. Metsue, A. Oudriss, J. Bouhattate, X. Feaugas, Contribution of the entropy on the thermodynamic equilibrium of vacancies in nickel, J. Chem. Phys. 140 (2014) 104705. https://doi.org/10.1063/1.4867543.

[32] A. Metsue, A. Oudriss, X. Feaugas, Hydrogen solubility and vacancy concentration in nickel single crystals at thermal equilibrium: New insights from statistical mechanics and ab initio

calculations, J. Alloys Compd. 656 (2016) 555–567. https://doi.org/10.1016/j.jallcom.2015.09.252.

[33] H.J. Monkhorst, J.D. Pack, Special points for Brillouin-zone integrations, Phys. Rev. B. 13 (1976) 5188–5192. https://doi.org/10.1103/PhysRevB.13.5188.

[34] R. Tran, Z. Xu, B. Radhakrishnan, D. Winston, W. Sun, K.A. Persson, S.P. Ong, Surface energies of elemental crystals, Sci. Data. 3 (2016) 160080. https://doi.org/10.1038/sdata.2016.80.

[35] M.C. Payne, M.P. Teter, D.C. Allan, T.A. Arias, J.D. Joannopoulos, Iterative minimizarion technoiques for ab initio total-energy calculations : molecular dynamics and conjugate gradients, Rev. Mod. Phys. 64 (1992) 1045. https://doi.org/10.1103/RevModPhys.64.1045.

[36] H. Jónsson, G. Mills, K.W. Jacobsen, Nudged elastic band method for finding minimum energy paths of transitions, in: Class. Quantum Dyn. Condens. Phase Simul., World Scientific, 1998: pp. 385–404. http://www.worldscientific.com/doi/abs/10.1142/9789812839664_0016 (accessed June 19, 2020).

[37] G. Henkelman, B.P. Uberuaga, H. Jónsson, A climbing image nudged elastic band method for finding saddle points and minimum energy paths, J. Chem. Phys. 113 (2000) 9901–9904. https://doi.org/10.1063/1.1329672.

[38] E. Wimmer, W. Wolf, J. Sticht, P. Saxe, C.B. Geller, R. Najafabadi, G.A. Young, Temperature-dependent diffusion coefficients from *ab initio* computations: Hydrogen, deuterium, and tritium in nickel, Phys. Rev. B. 77 (2008) 134305. https://doi.org/10.1103/PhysRevB.77.134305.

[39] X. Sha, B. Jackson, Ab initio and transition state theory studies of the energetics of H atom resurfacing on Ni(111), Chem. Phys. Lett. 357 (2002) 389–396. https://doi.org/10.1016/S0009-2614(02)00576-6.

[40] D. Di Stefano, M. Mrovec, C. Elsässer, First-principles investigation of quantum mechanical effects on the diffusion of hydrogen in iron and nickel, Phys. Rev. B. 92 (2015) 224301. https://doi.org/10.1103/PhysRevB.92.224301.

[41] G.A. Voth, Feynman path integral formulation of quantum mechanical transition-state theory, J. Phys. Chem. 97 (1993) 8365–8377. https://doi.org/10.1021/j100134a002.

[42] G. Alefeld, Hydrogen in metals. 1: Basic properties, Springer, Berlin, 1978.

[43] A. Hallil, A. Metsue, A. Oudriss, J. Bouhattate, X. Feaugas, Segregation energy of the hydrogen at Ni Σ3 grain boundaries: some implications of the atomic volume and the interstitial self-stress, J. Mater. Sci. 53 (2018) 5356–5363. https://doi.org/10.1007/s10853-017-1941-5.

[44] A. Metsue, A. Oudriss, X. Feaugas, Displacement field induced by a vacancy in nickel and some implications for the solubility of hydrogen, Philos. Mag. 94 (2014) 3978–3991. https://doi.org/10.1080/14786435.2014.975769.

[45] D. Guedes, A. Oudriss, S. Frappart, G. Courlit, S. Cohendoz, P. Girault, J. Creus, J. Bouhattate, A. Metsue, F. Thebault, L. Delattre, D. Koschel, X. Feaugas, The influence of hydrostatic stress

states on the hydrogen solubility in martensitic steels, Scr. Mater. 84–85 (2014) 23–26. https://doi.org/10.1016/j.scriptamat.2014.04.006.

[46] X. Zhou, D. Marchand, D.L. McDowell, T. Zhu, J. Song, Chemomechanical Origin of Hydrogen Trapping at Grain Boundaries in fcc Metals, Phys. Rev. Lett. 116 (2016) 075502. https://doi.org/10.1103/PhysRevLett.116.075502.

[47] S. Frappart, X. Feaugas, J. Creus, F. Thebault, L. Delattre, H. Marchebois, Hydrogen solubility, diffusivity and trapping in a tempered Fe–C–Cr martensitic steel under various mechanical stress states, Mater. Sci. Eng. A. 534 (2012) 384–393. https://doi.org/10.1016/j.msea.2011.11.084.

[48] H. Peisl, Lattice strains due to hydrogen in metals, in: Hydrog. Met. I, Springer, Berlin, 1978: pp. 53–73.

[49] R. Matsumoto, Y. Inoue, S. Taketomi, N. Miyazaki, Influence of shear strain on the hydrogen trapped in bcc-Fe: A first-principles-based study, Scr. Mater. 60 (2009) 555–558. https://doi.org/10.1016/j.scriptamat.2008.12.009.

[50] G. Hachet, A. Metsue, A. Oudriss, X. Feaugas, Influence of hydrogen on the elastic properties of nickel single crystal: A numerical and experimental investigation, Acta Mater. 148 (2018) 280–288. https://doi.org/10.1016/j.actamat.2018.01.056.

[51] L. Vitos, A.V. Ruban, H.L. Skriver, J. Kollár, The surface energy of metals, Surf. Sci. 411 (1998) 186–202. https://doi.org/10.1016/S0039-6028(98)00363-X.

[52] W.-B. Zhang, C. Chen, S.-Y. Zhang, Equilibrium Crystal Shape of Ni from First Principles, J. Phys. Chem. C. 117 (2013) 21274–21280. https://doi.org/10.1021/jp404569m.

[53] F. Mittendorfer, A. Eichler, J. Hafner, Structural, electronic and magnetic properties of nickel surfaces, Surf. Sci. 423 (1999) 1–11. https://doi.org/10.1016/S0039-6028(98)00892-9.

[54] J.-Y. Lee, M.P.J. Punkkinen, S. Schönecker, Z. Nabi, K. Kádas, V. Zólyomi, Y.M. Koo, Q.-M. Hu, R. Ahuja, B. Johansson, J. Kollár, L. Vitos, S.K. Kwon, The surface energy and stress of metals, Surf. Sci. 674 (2018) 51–68. https://doi.org/10.1016/j.susc.2018.03.008.

[55] G. Allan, J. Lopez, Influence of chemisorbed oxygen on nickel surface vibrations, Surf. Sci. 95 (1980) 214–226. https://doi.org/10.1016/0039-6028(80)90137-5.

[56] J.W.M. Frenken, R.G. Smeenk, J.F. van der Veen, Static and dynamic displacements of nickel atoms in clean and oxygen covered Ni(001) surfaces, Surf. Sci. 135 (1983) 147–163. https://doi.org/10.1016/0039-6028(83)90216-9.

[57] D.L. Adams, L.E. Petersen, C.S. Sorensen, Oscillatory relaxation of the Ni(110) surface: a LEED study, J. Phys. C Solid State Phys. 18 (1985) 1753–1766. https://doi.org/10.1088/0022-3719/18/8/021.

[58] H.C. Lu, E.P. Gusev, E. Garfunkel, T. Gustafsson, A MEIS study of thermal effects on the Ni(111) surface, Surf. Sci. 352–354 (1996) 21–24. https://doi.org/10.1016/0039-6028(95)01083-1.

[59] J. Lapujoulade, K.S. Neil, Chemisorption of Hydrogen on the (111) Plane of Nickel, J. Chem. Phys. 57 (1972) 3535–3545. https://doi.org/10.1063/1.1678790.

[60] A. Oudriss, J. Creus, J. Bouhattate, E. Conforto, C. Berziou, C. Savall, X. Feaugas, Grain size and grain-boundary effects on diffusion and trapping of hydrogen in pure nickel, Acta Mater. 60 (2012) 6814–6828. https://doi.org/10.1016/j.actamat.2012.09.004.

[61] A. Metsue, A. Oudriss, X. Feaugas, Trapping/detrapping kinetic rates of hydrogen around a vacancy in nickel and some consequences on the hydrogen-vacancy clusters thermodynamic equilibrium, Comput. Mater. Sci. 151 (2018) 144–152. https://doi.org/10.1016/j.commatsci.2018.05.013.

[62] S. Wright, J.F. Skelly, A. Hodgson, Energy disposal during desorption of D2 from the surface and subsurface region of Ni(111), Faraday Discuss. 117 (2000) 133–146. https://doi.org/10.1039/b004010j.

[63] H. Eyring, The Activated Complex in Chemical Reactions, J. Chem. Phys. 3 (1935) 107–115. https://doi.org/10.1063/1.1749604.

[64] C. Wert, C. Zener, Interstitial Atomic Diffusion Coefficients, Phys. Rev. 76 (1949) 1169–1175. https://doi.org/10.1103/PhysRev.76.1169.

[65] J. Li, A. Oudriss, A. Metsue, J. Bouhattate, X. Feaugas, Anisotropy of hydrogen diffusion in nickel single crystals: the effects of self-stress and hydrogen concentration on diffusion, Sci. Rep. 7 (2017) 45041. https://doi.org/10.1038/srep45041.

[66] C. Lekbir, Effet de la déformation plastique du nickel monocristallin sur l'état d'équilibre de l'hydrogène en surface et subsurface, La Rochelle University, 2012.

[67] S.Y. Kim, I.-H. Lee, S. Jun, Transition-pathway models of atomic diffusion on fcc metal surfaces. II. Stepped surfaces, Phys. Rev. B. 76 (2007) 245408. https://doi.org/10.1103/PhysRevB.76.245408.

[68] J.C.M. Li, R.A. Oriani, L.S. Darken, The Thermodynamics of Stressed Solids, Z. Für Phys. Chem. 49 (1966) 271–290. https://doi.org/10.1524/zpch.1966.49.3_5.271.

[69] R. Nazarov, T. Hickel, J. Neugebauer, *Ab initio* study of H-vacancy interactions in fcc metals: Implications for the formation of superabundant vacancies, Phys. Rev. B. 89 (2014) 144108. https://doi.org/10.1103/PhysRevB.89.144108.

[70] G. Hachet, Multi-scale investigation of the consequences of hydrogen on the mechanical response of cyclically strained nickel single crystal, La Rochelle University, 2018.

[71] Y.-W. You, X.-S. Kong, X.-B. Wu, Y.-C. Xu, Q.F. Fang, J.L. Chen, G.-N. Luo, C.S. Liu, B.C. Pan, Z. Wang, Dissolving, trapping and detrapping mechanisms of hydrogen in bcc and fcc transition metals, AIP Adv. 3 (2013) 012118. https://doi.org/10.1063/1.4789547.

[72] V.B. Shenoy, Atomistic calculations of elastic properties of metallic fcc crystal surfaces, Phys. Rev. B. 71 (2005) 094104. https://doi.org/10.1103/PhysRevB.71.094104.

[73] R. Kirchheim, J.P. Hirth, Stress and solubility for solutes with asymmetrical distortion fields, Acta Metall. 35 (1987) 2899–2903. https://doi.org/10.1016/0001-6160(87)90288-4.

[74] F.C. Larche, J. l. Cahn, The effect of self-stress on diffusion in solids, Acta Metall. 30 (1982) 1835–1845. https://doi.org/10.1016/0001-6160(82)90023-2.

[75] S. Taketomi, R. Matsumoto, N. Miyazaki, Atomistic study of hydrogen distribution and diffusion around a {112} edge dislocation in alpha iron, Acta Mater. 56 (2008) 3761–3769. https://doi.org/10.1016/j.actamat.2008.04.011.

[76] J.C. Dyre, Dominance of shear elastic energy far from a point defect in a solid, Phys. Rev. B. 75 (2007) 092102. https://doi.org/10.1103/PhysRevB.75.092102.